POLITECNICO DI TORINO

Master's Degree in Energy and Nuclear Engineering

Master's Degree Thesis

Modeling of a receiver coupled with PCM thermal storage in a solar concentration system

Supervisor

Prof. Davide PAPURELLO

Candidate

Federico ARIANO

March 2024

Summary

In the perspective of transitioning from fossil fuels, diversifying energy production, and providing an alternative to critical materials, the following thesis aims to analyze a solar receiver, exploring thermal energy storage technologies.
The system under consideration is the dish solar concentrator located at the Energy Center, where measurements were conducted using different receiver materials. After the data collection from the receiver and the analysis of the various materials, the next step involved the modeling on COMSOL Multiphysics, which allowed the visualization of the thermal behavior of the receiver and the temperature distribution. Following this, an attempt was made to integrate the basic model with thermal storage using various phase change materials and to find an optimal configuration of operation and internal arrangement.
Thermal energy storage systems (TES) represent a technology that has not yet been adequately exploited to date. Compared to electric storage systems, they offer greater flexibility of use and longevity. Futhermore, in most cases, they can entail lower costs, a shorter energy conversion cycle and an easier integration in thermal applications. TES systems have not yet reached technological maturity also because they involve a wide range of materials and engineering solutions, with a greater complexity in terms of development and standardization.
Eventually, the study proposes a system for managing the PCM within the receiver, allowing for charging and discharging processes, while also integrating the solar concentration system with an Organic Rankine Cycle, enabling the conversion of heat from the solar concentrator, operating at medium-low temperatures, into electricity. The objective was to decouple solar energy availability from the final electricity generation process, thereby ensuring a more reliable and consistent energy supply.

Table of Contents

List of Tables

List of Figures

Chapter 1

Introduction

1.1 Energy Outlook

In the contemporary global context, the challenges presented by climate change demand highly effective solutions. However, these solutions must encompass environmental, social, and economic considerations, adding layers of complexity. Climate change's secondary effects encompass extreme weather events, biodiversity loss, rising sea levels, and territorial desertification, leading to reduced access to clean water and arable land, and an upsurge in climate refugees. Central to addressing these challenges is the concept of **sustainable development**, introduced in the *1987 Brundtland Report* as "development that meets present needs without compromising the ability of future generations to meet their own needs" [1]. This definition is very generic, as it's challenging to objectively estimate current and future needs, but it serves as a guiding framework for decision-making in various fields, considering the consequences of long-term actions and taking into account the importance of equity and social justice. In terms of raising awareness about global warming and ensuring access to scientific evidence, the Copernicus Climate Change Service (C3S), an initiative executed by the European Centre for Medium-Range Weather Forecasts, plays a crucial role. It consistently releases monthly climate bulletins detailing changes observed in global surface air temperature, sea ice extent, and hydrological parameters, making it a significant tool in addressing climate change. In Figure 1.1, the temperatures of the hottest boreal summers since 1940 are depicted. The summer of 2023 stands as the **warmest summer ever recorded** with a global-mean surface air temperatures of 16.77°C, 0.66°C above average and 0.29°C above the previous hottest summer, 2019 [2]. Across time, also thanks to the type of evidence and data shown previously, the scientific community has increasingly reached consensus that climate change is primarily attributed to anthropogenic activities. One of the latest studies, *"Consensus revisited: quantifying*

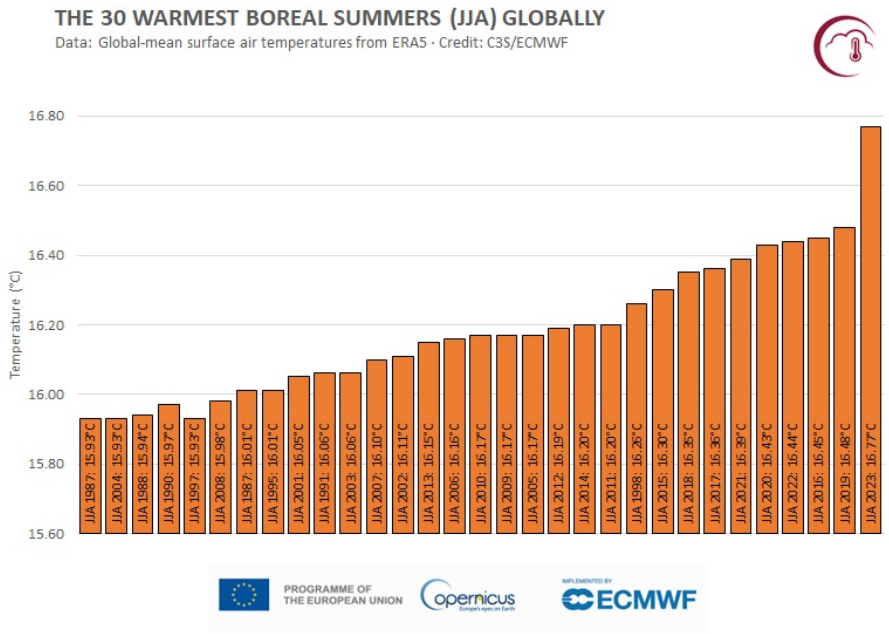

Figure 1.1: Global-mean surface air temperatures for the 30 warmest boreal summers (June-July-August) in the ERA5 data record, ranked from lower to higher temperature [2]

scientific agreement on climate change and climate expertise among Earth scientists 10 years later" (Krista F Myers et al 2021), confirmed that among 153 climate experts who were independently verified, 98.7% concurred that the Earth's warming trend is mainly caused by human activities, the primary of which is the combustion of fossil fuels. It is shown in Figure 1.2, where each bar represents a single author's publication history from 2015 to 2019, grey bars show total number of publications in all fields, and colored bars in foreground show total number of publications that were coded as 'climate relevant'. In addition, the percentage increases even more for the ones with the highest level of expertise (which have published 20+ peer reviewed papers between 2015 and 2019), arriving to a 100% agreement on the human-related origin of the warming [3]. **The United Nations Framework Convention on Climate Change (UNFCCC)** was held each year since June 1992 with the main goal of "stabilization of greenhouse gas concentrations in the atmosphere at a level that would prevent dangerous anthropogenic interference with the climate system. Such a level should be achieved within a time-frame sufficient to allow ecosystems to adapt naturally to climate change, to ensure that food production is not threatened and to enable economic development to proceed in a sustainable manner" [4]. Over the years, the convention has expanded to include

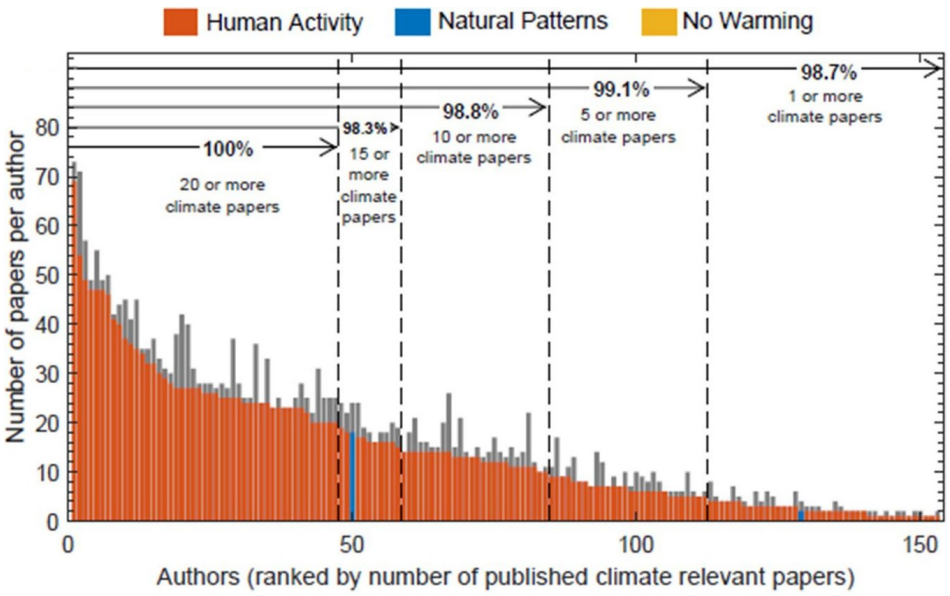

Figure 1.2: Histogram of climate field authors who believe that global warming primarily stems from human activities or natural patterns [3]

an increasing number of countries. Presently, it hosts representatives from 197 countries and welcomes 70,000 delegates. Although from the beginning, conferences have consistently been heavily influenced by socio-political and economical factors, at the 2023 "Conference of the Parties of the UNFCCC", also known as "**COP28**", there have been important steps forward concerning the global awareness on climate change. The president of the commission, the executive of the Emirati oil company Adnoc, has been the most determined opponent of a phaseout from oil and gas, but some countries such as Australia, the US, the UK, Canada and Japan, went against him stating that they wouldn't sign an agreement that would be a "death certificate" for small islands (due to the subsequent rise in water level) [5][6][7]. The international deal which was finally approved aims at countering the rising of global temperatures in line with 1.5°C guidelines, also to meet the goals of Paris Agreement; paying attention to the following global efforts [8]:

- "**Tripling renewable energy capacity** globally and doubling the global average annual rate of energy efficiency improvements by 2030;
- Accelerating efforts towards the phase-down of unabated coal power;
- Accelerating efforts globally towards **net zero emission energy systems**, utilizing zero- and low-carbon fuels well before or by around mid-century;
- **Transitioning away from fossil fuels** in energy systems, in a just, orderly

and equitable manner, accelerating action in this critical decade, so as to achieve net zero by 2050 in keeping with the science;

- **Accelerating zero- and low-emission technologies**, including, inter alia, renewables, nuclear, abatement and removal technologies such as carbon capture and utilization and storage, particularly in hard-to-abate sectors, and low-carbon hydrogen production;
- Accelerating and substantially reducing non-carbon-dioxide emissions globally, including in particular methane emissions by 2030;
- Accelerating the reduction of emissions from road transport on a range of pathways, including through development of infrastructure and rapid deployment of zero-and low-emission vehicles;
- Phasing out inefficient fossil fuel subsidies that do not address energy poverty or just transitions, as soon as possible"

All the global efforts can be gathered together in two main conceptual paths, which can be summarised in:

a) Moving away from sources of carbon emissions, coal and fossil fuels power or heat generation, transport, and also non-carbon-dioxide emissions such as methane

b) Improving renewable energy capacity and efficiency, with a wider diffusion of abatement and removal technologies, and low-carbon fuels

The main goal of the agreement is to reach the net zero emissions by 2050, which are the balance between the amount of greenhouse gases emitted and captured in the atmosphere, but it should be done allowing for stability in energy supply and economic growth especially for emerging countries. From the other side, a loss and damage fund has been established for the most vulnerable countries, which will be the ones most affected by the future effects of the climate change, in order to be resilient to the impacts of climate change [9]. The focus on renewable energy is very strong, as the main approach to lead a shift towards decarbonised energy production. Furthermore, for the first time in the agreement it was formally recognised also the role of nuclear energy to meet the goals of the Paris Agreement [1] as one of

[1]The Paris Agreement, established during the UN Climate Change Conference (COP21) in Paris, was adopted by 196 Parties, officially coming into effect on November 4, 2016. The primary objective of the Paris Agreement is to restrain the rise in the global average temperature to below 2°C above pre-industrial levels, with a further ambition to limit the increase to 1.5°C. In particular, achieving the 1.5°C target limits a peak in greenhouse gas emissions no later than 2025 and a subsequent reduction of 43% by the year 2030 [10]

the accelerating zero- and low-emission technologies [11]. It is also necessary to highlight that the COP28 agreement is a voluntary commitment, and doesn't carry any legal obligations. Therefore, the true effectiveness of these agreements in achieving the phase-out has been questioned, some view it as a significant step forward in awareness, whereas others see it merely as a superficial effort. The international community, always within the framework of the United Nations, has also aligned its efforts with the **Sustainable Development Goals (SDGs)**. The SDGs are a universal call to action in 17 goals to "improve health and education, reduce inequality, and spur economic growth" by 2030 [12]. These goals intersect with climate change mitigation and adaptation efforts, emphasizing the importance of sustainable development in addressing environmental challenges. From an energy

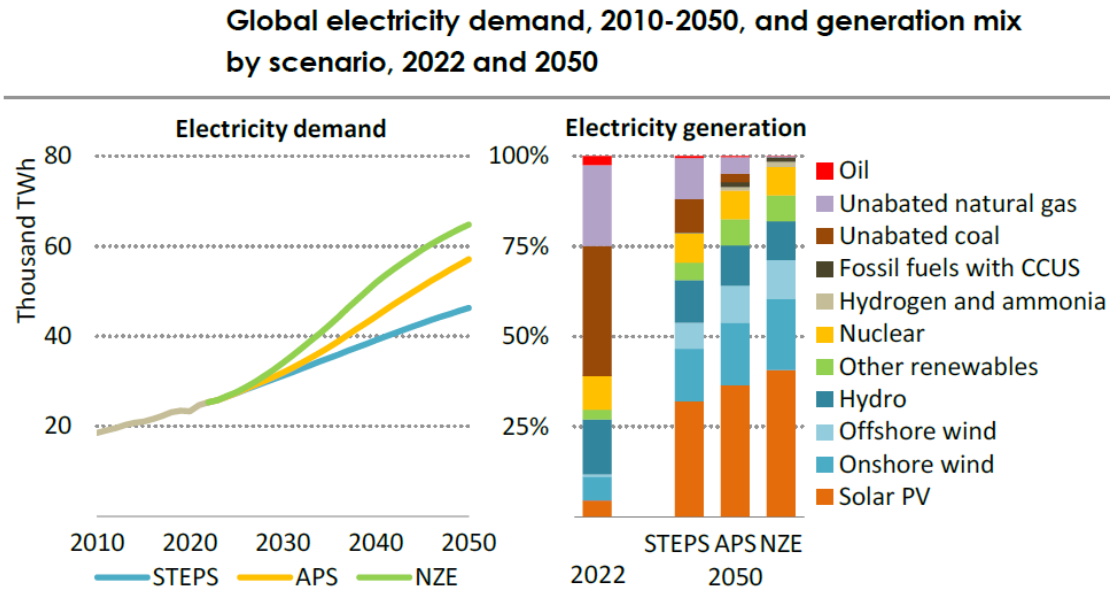

Figure 1.3: Electricity demand and the generation mix according to the STEPS, APS, NZE scenarios, considering as "Other renewables", concentrating solar power, bioenergy and renewable waste, geothermal and marine power [13]

point of view, it's important to take into account the substantial growth of the global population. The global electricity demand will rise in the next years according to different scenarios, pushed by factors such as population and income growth, with an increase of over 80% in the STEPS, 120% in the APS, and 150% in the NZE Scenario[2] (Figura 1.3). The percentage on the total mix of unabated fossil fuels will decrease significantly, while the **annual increase of renewables** is

[2]The STEPS, APS, and NZE scenarios constitute the three primary projections for the evolution of the energy sector. The first scenario is characterized by a more conservative approach,

estimated to be **3-9%** by 2030 and in general the low-emission sources are set to rise substantially across all scenarios [13]. In this growth perspective, it's crucial to invest in various forms of green energy that can meet the different needs of specific communities, increasing the diversification of energy sources and thus reliability, security, and self-sufficiency in energy production.

acknowledging the possibility that not all climate goals will be achieved. On the other hand, the second scenario assumes the in time fulfillment of all carbon reduction commitments, whereas the third scenario envisions the attainment of net-zero emissions of CO2 by 2050 through global collaboration

Chapter 2

Concentrated solar power

2.1 Solar Energy

The sun represents an abundant and inexhaustible resource that could provide a clean and environmental friendly alternative to other high-carbon fuels. Potentially, the solar energy reaching Earth annually exceeds the one present in fossil resources, and it surpasses the amount required for the world's annual consumption by far (Figure 2.1). Employing the **full potential of solar energy** through proper

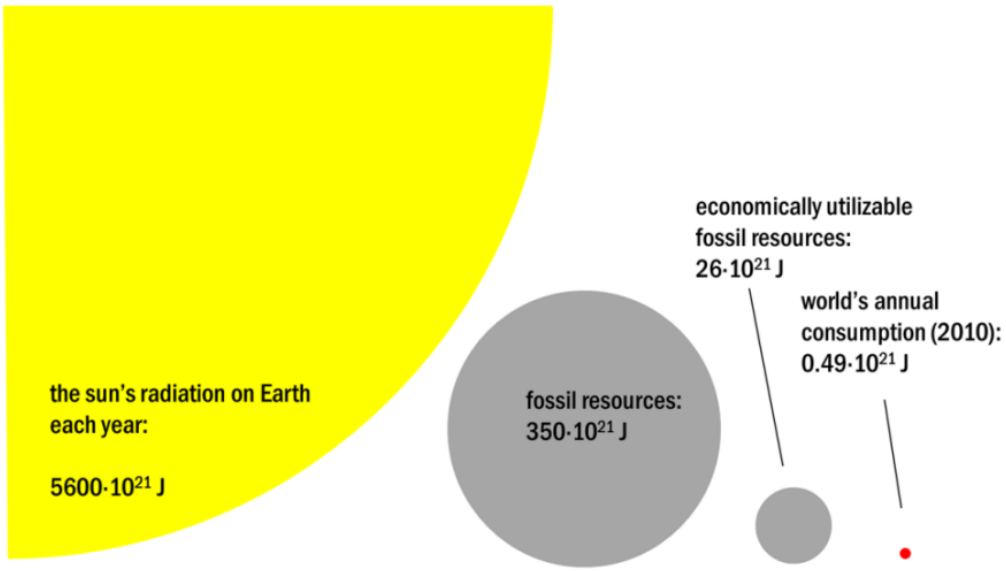

Figure 2.1: Comparison between world energy solar and fossil resources and world primary energy consumption [14]

exploitation could be an enormous step forward towards a more sustainable way to

conceive the way we power our world. Still today, when observing at the overall usage of energy forms, solar and wind energy (also the latter derives from the sun) still play a relatively marginal role (Figure 2.2). Prioritizing the development and utilization of solar energy turns out to be a fundamental pathway toward achieving global sustainable goals. Within this framework, concentrated solar power (CSP) technologies have the potential to significantly enhance the efficiency and scalability of solar energy utilization, also displaying a remarkable potential for growth.

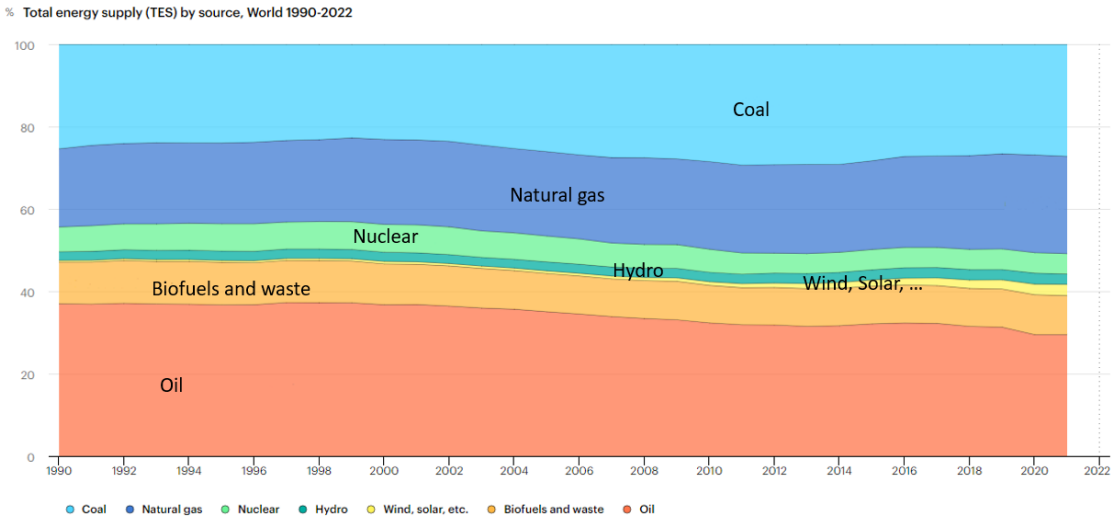

Figure 2.2: % of Total Energy Supply (TES) for different sources, World 1990-2022 [15]

2.2 Concentrated Solar Power Technologies

Concentrated Solar Power technologies focus solar rays using mirrors and lenses, directing them toward a small surface heated to high temperatures. The surface responsible for concentrating the rays onto a surface is the reflector, whereas the receiver absorbs the radiation and transmits thermal energy to a heat transfer fluid. There are currently four main technologies in the field of concentrated solar power, two of which, the parabolic trough and the solar tower, have have found commercial success. The primary categorization can be done on how they focus the sun rays:

- **Line-focusing systems**, which concentrate sunlight onto a linear receiver (Figure 2.3):
  - Parabolic Trough
  - Linear Fresnel

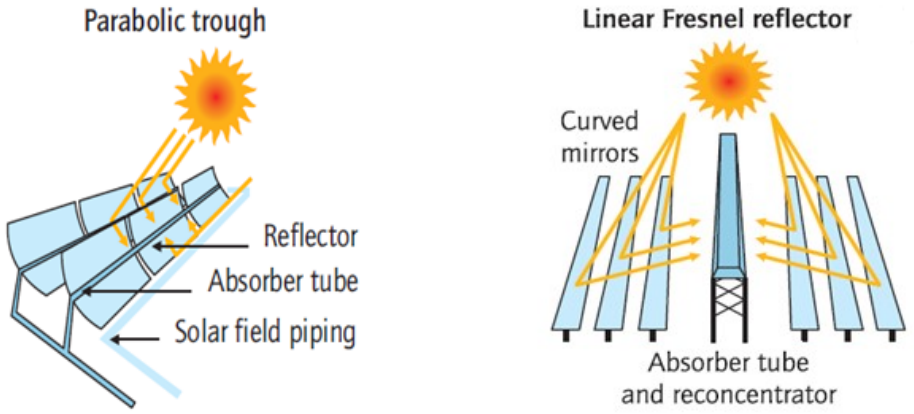

Figure 2.3: Line-focusing systems [16]

- **Point-focusing systems**, that concentrate sunlight from a large area onto a small, specific point (Figure 2.4):
  - Central Receiver
  - Parabolic Dish

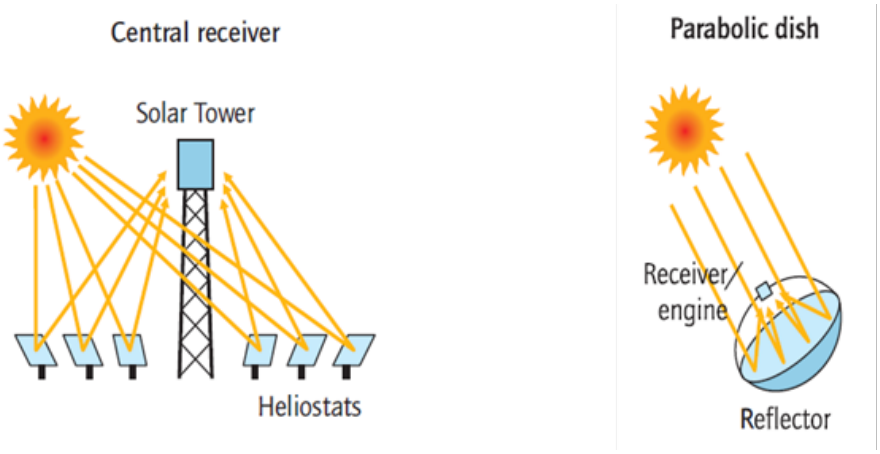

Figure 2.4: Point-focusing systems [16]

In Table 2.1, the various characteristics for each technology are indicated. In particular, the maximum temperature and the maximum efficiency are calculated for ideal conditions, 100% concentration efficiency and a black body.

Solar System	Concentr. Ratio	Operation Temp. (°C)	Therm. Eff. (%)	Solar to Elect. Eff. (%)
Parabolic Trough	15-45	300–550	Low	12–15
Linear Fresnel	10-40	250–550	Low	8–10
Central Receiver	100-1000	300–1000	High	20–30
Parabolic Dish	150-1500	400–1500	High	20–30

Table 2.1: Characteristics of Solar Technologies [17]

2.3 Parabolic Trough Collector (PTC)

Parabolic troughs are systems which use paraboloid shaped reflectors to focus solar radiation to a central tubular absorber tube. The tube, which is placed at the focal line, is made out of different metallic and ceramic layers and contains a working fluid which is heated to high temperature. The fluid than powers a heat engine that drives a generator, producing electricity. The heat transfer fluid can be oil, water, or molten salts, the latter of which is still under research due to its primary challenge, a high freezing point ranging from 120 to 220°C. However, it is becoming more and more employed because it allows for operation at higher temperatures, typically between 450 and 550°C. Due to its longer commercial operations and reduced exposure to technical and financial risks, the PTC stands as the prevailing technology in current usage within Concentrated Solar Power plants [18].

2.4 Linear Fresnel Reflector (LFR)

The Linear Fresnel Reflector is composed of a linear array of mirrors parallel to the symmetry axis that concentrates the sunlight onto a central line receiver. Thus, even with a lower optical reflection quality, it is a simpler and cheaper collector system than the one from the Parabolic Trough, which has a complex shape manufacturing. It is also present a secondary concentrator above the receiver, which permits to correct optical mistakes by increasing the concentration factor. The tracking system is necessary to adjust the mirror inclination to always collect the direct radiation during the sun's path. However, this system has not been widely exploited mainly because of its lower optical efficiency and temperature operation, and also for lower expertise [19].

2.5 Solar Power Tower (SPT)

The Solar Tower technology consist of a field of mirrors known as heliostats, which concentrate sunlight to a receiver placed on top of a tower. The heliostats, are strategically positioned to track the sun and present a two-axes tracking system. In the receiver there is a heat transfer fluid, which can be water, directly used in the steam cycle, or an intermediate one like molten salts for transferring heat in a heat exchanger. The generated steam is then used to drive a turbine connected to an electric generator, producing electricity. The solar receiver can achieve high temperatures above 1000 K, ensuring a high cycle efficiency, mainly for this reason, central tower plants are considered the most promising CSP technology in the coming years [20].

2.6 Parabolic dish collector (PDC)

The parabolic dish is a concentrating system that uses a dish shaped reflector to focus the sunlight onto a focal central point, upon which a receiver is located. The receiver captures incoming radiation, transforming it into heat that is then transferred to a heat transfer fluid, used for the generation of heat or electricity. The

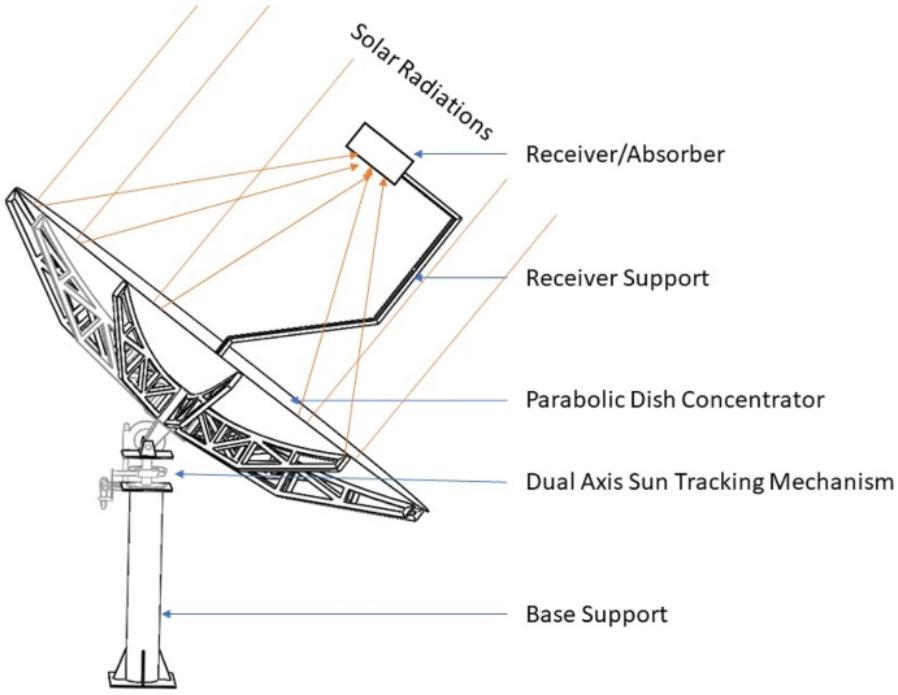

Figure 2.5: Parabolic Dish Schematic [21]

solar dish system's receiver acts as the intermediary connecting the concentrator and the engine. Its dual functionality involves absorbing a significant portion of reflected radiation from the collector and transforming it into heat, followed by the transmission of this heat to the working gas of the heat engine. The material is chosen searching for elevated absorption rates and efficient heat transfer characteristics. The schematic of the parabolic dish is shown in Figure 2.5. The main field of improvement for the parabolic dish is its efficiency in concentrating solar power and converting it into heat. This could be achieved by improving the tracking mechanism, also paired with artificial intelligence, find advanced reflective coating materials and optimizing receiver design to minimize losses. Furthermore, the integration in the system of a storage system with the proper heat transfer fluid is crucial for a better exploitation of the converted energy and the best energy utilization downstream.

2.6.1 Concentrator

The collector is a curved reflective surface, geometrically represented by a section of a rotational paraboloid. The mirror possesses a geometrical focal point where incident radiation is concentrated thanks to the shape of the surface. One of the main factors which characterize the collector is the *Concentration Ratio*, with A_{ap} the aperture area, the flat projection of the area of the dish, and A_{im}, the focal spot area (Figure 2.6). It can be expressed as follow as a geometrical mean:

$$C_{\text{r}} = \frac{A_{\text{ap}}}{A_{\text{im}}} \tag{2.1}$$

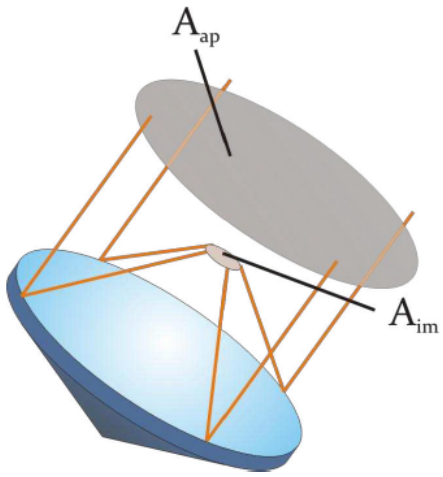

Figure 2.6: Aperture and Focal Spot areas [22]

It represents the ability to concentrate the solar rays onto a smaller focal surface, and therefore the increase of the initial solar irradiance. However, it is an approximation of the real mean radiation concentration, since it doesn't take into account the real reflectivity of the mirror, the scattering effect due to imperfections and the shading effect of the receiver and its support [22]. Another crucial parameter to

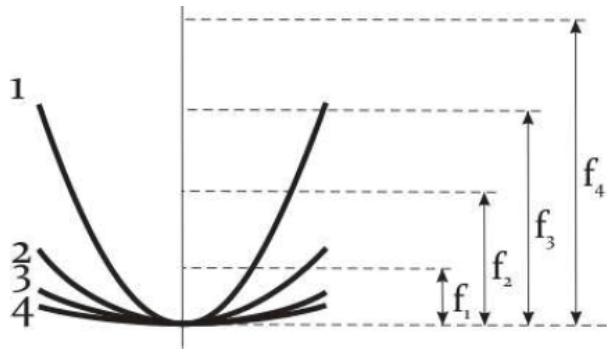

Figure 2.7: Difference in dish shape with focal length variation [22]

characterize the system is the *Focal Lenght*, which is the distance from the center of the dish to its focal point. It indicates how curved the dish is in relation to its diameter (Figure 2.7). This parameter is important for the precise placement of the receiver, ensuring maximum exposure to concentrated sunlight and avoiding as much as possible deviation from the optimal configuration. The focal length is the parameter for the mathematical expression with z axis coinciding with the one of the circular paraboloid [22]:

$$x^2 + y^2 = 4fz \tag{2.2}$$

However, if you want to characterize the solar dish only based on its shape and

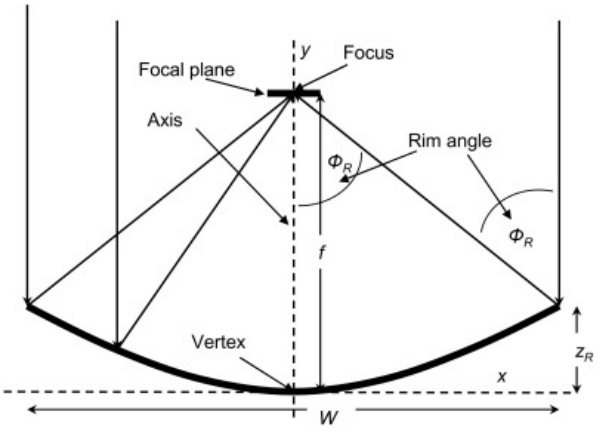

Figure 2.8: Schematic of a parabolic dish geometric dimensions [23]

not its absolute size, a useful parameter is the *Rim Angle* ϕ, which refers to the angle formed by the rim or edge of the dish relative to the horizontal plane (Figure 2.8). The combination of the two parameters totally determines the dish geometry, in shape and size (Figure 2.9). It can be also expressed in a correlation with d, the aperture diameter of the collector [22]:

$$\tan(\phi) = \frac{\frac{d}{f}}{2 - \frac{1}{8}(\frac{d}{f})^2} \tag{2.3}$$

Lastly, all those parameters can be grouped in a final equation:

$$\frac{d}{f} = -\frac{4}{tan\psi} + \sqrt{\frac{16}{\tan^2 \psi} + 16} \tag{2.4}$$

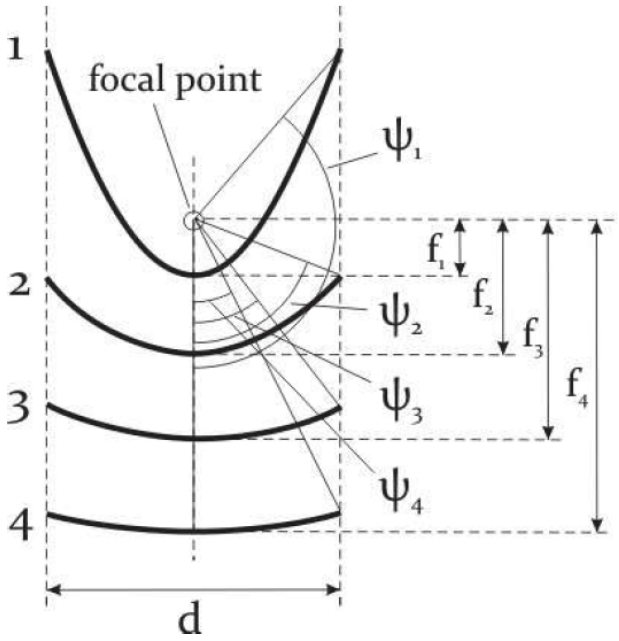

Figure 2.9: Relation between the rim angle and the focal length with same dish diameter [22]

Small rim angles cause the focal spot to widen, resulting in a reduction of the concentration ratio due to the increased focal distance. Instead, large rim angles cause the focal spot to narrow as a result of the tilted incidence of the reflected rays on the focal plane. The ideal rim angle to achieve high concentration ratio is 45° [22].

2.6.2 Tracking Mechanism

The tracking system can be single-axis or dual-axis.

- The **single-axis** allows to move only on one axis, which is typically vertical or horizontal. The horizontal axis tracking system is more efficient for following the sun's movement from east to west, while the vertical axis tracking system is ideal for locations where there is significant variation in the sun's elevation. This system is chosen for its economical affordability and simplicity.

- The **dual-axis** provides the highest efficiency, because it can track much more precisely the the sun's path, aiming at aligning the optical axis and the sun's direct radiation. It can be divided in [22]:

  – **Polar Tracking**: It is based on the displacement over *Declination* and *Hour Angle*. The former is the tilt angle from Earth's rotational axis, while the latter represents the time elapsed since noon in a location, perpendicular to the axis. They can be evaluated as:

  $$\delta = 23.45° \cdot \sin\left(\frac{360}{365} \cdot (n + 10)\right) \tag{2.5}$$

  n is the day of the year, starting from the January the 1st.

  $$h = 15 \cdot (T_{\mathrm{ST}} - 12) \tag{2.6}$$

  where the T_{ST} is the local solar time and the factor 15 converts the time difference from hours to degrees, as the Earth rotates 15 degrees per hour

  – **Altitude-Azimuth Tracking**: This method has a different reference system, based on *Altitude* and *Azimuth*. Altitude is measured vertically from observer's horizon, going from the 0° at horizon to 90° at the zenit:

  $$\alpha(t) = \arcsin\left(\sin(\delta)\sin(\phi) + \cos(\delta)\cos(\phi)\cos(h(t))\right) \tag{2.7}$$

  where ϕ is the latitude. Azimuth is the angle between the sun position around a vertical axis, ranging from 0° or 360° at the north and 180° at the south.

  $$\gamma(t) = \mathrm{sign}(\omega(t)) \left|\arccos\left(\frac{\sin(\alpha)\sin(\phi) - \sin(\delta)}{\cos(\alpha)\cos(\phi)}\right)\right| \tag{2.8}$$

  the sign function is +1 if ω is positive and -1 if it is negative [22].

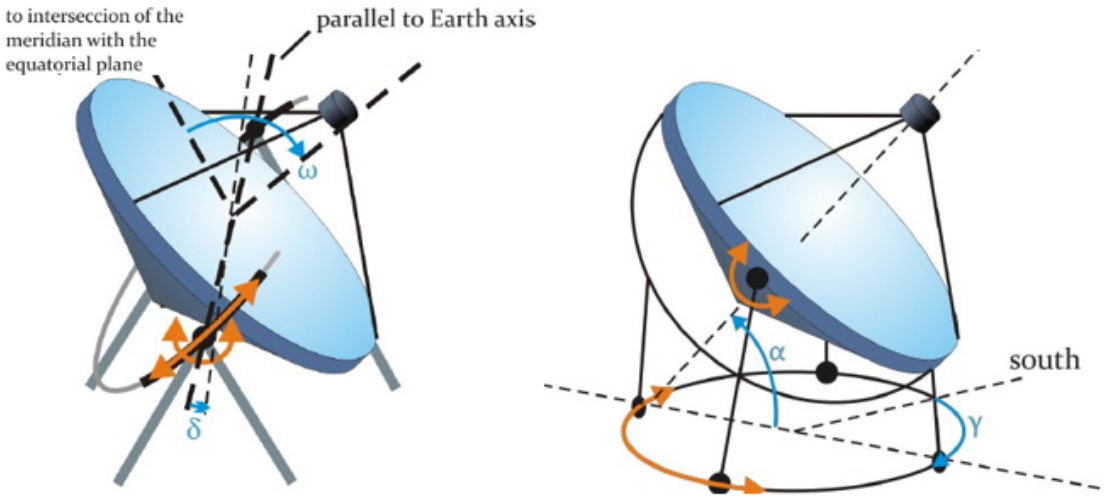

Figure 2.10: Schematic of the two dual-axis tracking configurations [22]

2.6.3 External and Cavity Receiver

External and cavity are two of the main technologies for a receiver. The external one is exposed directly to sunlight from various directions, while the cavity presents a chamber with an aperture at the focal point of the receiver. The schemes of functioning can be seen in Figure 2.11.

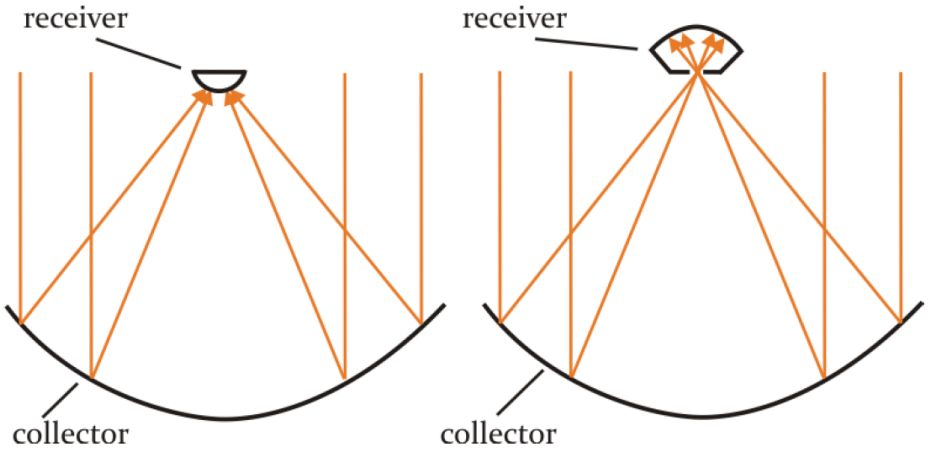

Figure 2.11: External and Cavity receiver schematic view [22]

The former is mechanically simpler, and has advantages in terms of maintenance and cost while the latter requires more complex engineering due to enclosed structure and higher temperatures. While an external receiver captures radiation from various directions and may be advantageous for collectors with a large rim

angle, it suffers from high heat losses, especially radiative losses, at the elevated operating temperatures of dish systems. In contrast, a cavity receiver, with its aperture directed only towards the vertex of the collector, experiences lower radiative heat losses. The concave shape of the absorber surface in a cavity receiver allows a significant portion of emitted radiation to be absorbed within the cavity, reducing total radiative heat loss. In addition, convective heat loss is lower in cavity receivers compared to unprotected external receivers. The aperture, typically at the focus of the concentrator, directs the highly concentrated flux into the cavity before reaching the larger absorbing surface area. This distribution minimizes the incident flux on the absorber surface, preventing thermal overstress on materials. Therefore, cavity receivers exhibit favorable absorption characteristics with minimal thermal losses. Due to these advantages, dish/Stirling systems exclusively use cavity receivers, while external receivers find application in parabolic dish systems operating at lower temperatures [22].

Tubular Receiver

Tubular absorber is a kind of external receiver which can operate with either gas or liquids as heat transfer fluids. It is constructed from a hollow cylindrical tube, typically made of a high-temperature resistant material such as steel, ceramics, or refractory metals. The outer surface of the cylinder may have a selective coating

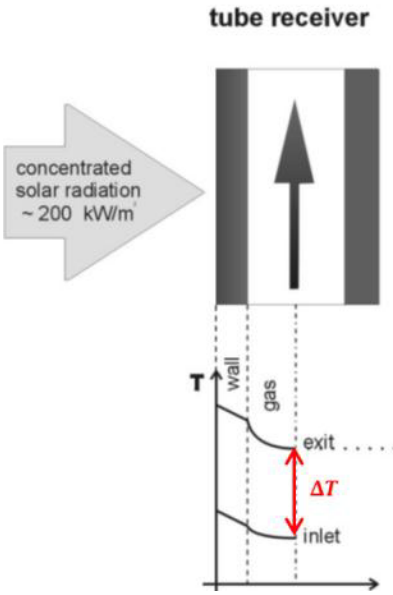

Figure 2.12: Tubular receiver and inlet and outlet temperature distribtion of the radius [24]

or absorber material designed to efficiently absorb solar radiation, enhancing the absorption of sunlight while minimizing heat loss through radiation. Inside the tubular receiver the transfer fluid flows, absorbing heat generated by concentrated solar radiation and transferring it for thermal or power generation applications. The inlet and the outlet is connected to piping which link the receiver to the other components of the solar concentration system. Other processes involved could be desalination, chemical manufacturing, district or water heating, air conditioning. In Figure 2.12, the schematic of the receiver is shown. The solar radiation reaches the external tube, the heat is transferred by conduction through the wall and heats the fluid, creating a differential in temperature between the inlet and outlet. The fluid temperature increases as one approaches the surface irradiated by the sunlight. With gas as a fluid, the limiting factor for the temperature is the low heat transfer coefficient with the walls [25]. The basic and the easiest heat transfer fluid is air, but it can be used also water/steam, molten nitrate salt, fluoride salts, liquid sodium. The main benefit of molten salts is that they can be both the heat transfer fluid and the storage medium, eliminating the necessity of an intermediate heat exchanger, but could be problematic for salt decomposition at high temperatures (600-630°C). The liquid sodium, on the other hand, has the main benefit in the very high exchange coefficient, allowing for a higher heat removal, reducing thermal stresses [25][26].

2.6.4 Errors reducing concentrations

Many factors can influence the perfect concentration of the solar dish, among these [23]:

- **Specularity error**: It is the deviation of reflected light from the ideal reflection, due to the material not being an ideal mirror. It can be represented as σ_{sp}, standard deviation of the distribution of reflected ray angles.

- **Surface slope error**: Error due to the variation in the slope of the surface with respect to the ideal curvature. It can happen due to manufacturing imperfections, intrinsic material properties or environmental degradation. It is σ_{sl}, standard deviation of angular change of surface normal vectors with respect to ideal direction.

- **Alignment error**: Due to the imperfect assembling of the different pieces which constitute the final concentrator. σ_{al} is the standard deviation in normal angles with respect to this alignment errors.

- **Tracking error**: Error arising from flaws of the tracking system, that being an estimation of the sun's path, does not allow a perfect alignment with

respect to the sun. σ_{tr} can be a tracking error, evaluated over a sufficient period of time.

In general, all those terms can be gathered in a normal distribution of all errors, as the sum of the squares of the components under square root. There's an angle doubling effect for the surface orientation effect [27]:

$$\sigma_{\text{tot}} = \sqrt{\sigma_{\text{sp}}^2 + 4\sigma_{\text{sl}}^2 + 4\sigma_{\text{al}}^2 + \sigma_{\text{tr}}^2} \tag{2.9}$$

However, the accuracy of the standard deviation errors varies among different types, and as a result, the total error may not be entirely accurate. Moreover, other indirect factors can also have a significant influence on the perception of errors. Wind, for example, can exert a significant load on the structure and over time could exacerbate certain errors such as alignment or tracking errors if the structure's zero reference were to be altered.

2.6.5 Receiver Losses

Radiative losses

The first source of loss is the radiative one, which at high temperatures can be more decisive than the others. It includes both the emitted radiation and the reflection of the incoming radiation. For what concerns the reflection, some of the main factors besides the material and the coating is the geometry of the receiver and the incidence angle of light. Instead, the radiation is mainly linked to the Stefan-Boltzmann Law, which states that every body with a temperature above the absolute zero, emits radiation with the following behaviour:

$$\dot{Q}_{\text{rad}} = \varepsilon \sigma A T^4 \tag{2.10}$$

In the equation the ϵ is the emissivity of a grey body, approximated constant in the wavelength and ranging from 0 to 1, $\sigma = 5.67 \cdot 10^{-8}$ $\frac{W}{m^2 \cdot K^4}$ is the constant of proportionality, the Stefan–Boltzmann constant, A is the emitting area of the body. The emissivity can be determined experimentally using a spectrometer or by theoretical calculations. The emitted radiation is dependent on the intrinsic characteristics of the material and proportional to the forth power of the temperature. For this last reason, the more the temperature rises, the more it becomes relevant in the losses balance and needs counteractions to be reduced. The cavity receivers reduce this kind of losses allowing for a partial reabsorption of the emitted radiation. For what concerns the selective coatings, they are not commonly used in high temperature systems because they degrade rapidly in a high flux environment and work less effectively due to the overlap between the absorbed and the emission spectrum [22]. In a simplified model, with the T_{rec} the average temperature of the receiver, the

loss by emitted radiation towards the surrounding environment can be expressed as follows:

$$\dot{Q}_{\text{rad}} = \varepsilon\sigma A(T_{\text{rec}}^4 - T_{\text{amb}}^4) \tag{2.11}$$

Convection Losses

Convection losses refer to the heat energy lost from the receiver due to the transfer of heat to the surrounding fluid by convection, in this case air. The main source of loss is the action of wind, which can be considered an external forced convection, but also of the natural convection of heated surrounding air (it becomes less dense and tends to rise, while cooler, denser fluid sinks to replace it, creating a convection current). Convection losses occur primarily due to the temperature difference between the receiver and the surrounding medium. According to *Newton's law*, the rate of heat transfer by convection is proportional to the temperature difference between the surface and the surrounding fluid or gas:

$$\dot{Q}_{\text{conv}} = hA(T_{\text{rec}} - T_{\text{amb}}) \tag{2.12}$$

where the heat transfer coefficient $h\left[\frac{W}{m^2 \cdot K}\right]$, is calculated by empirical correlations and depending on the property of the fluid (such as viscosity, density, and thermal conductivity), the flow regime and direction, the surface geometry. The more the fluid velocity and the receiver temperatures are high, the more the convection losses will be important. Some measures to reduce these kind of losses could include

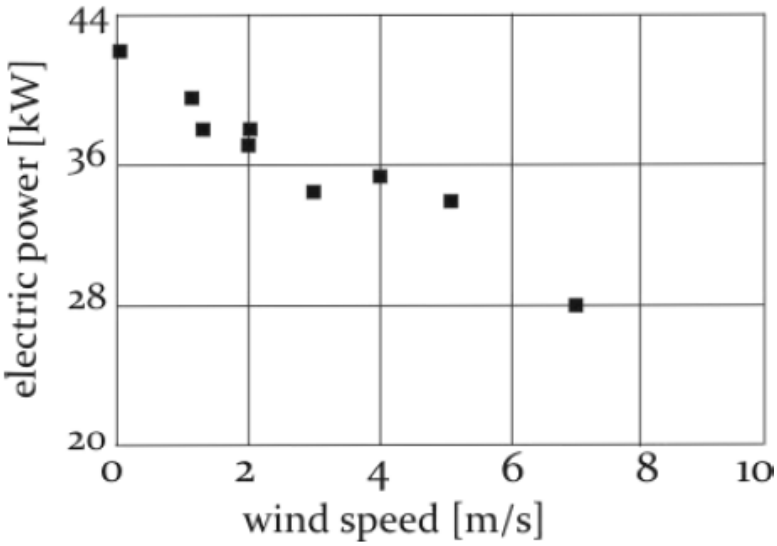

Figure 2.13: Influence of wind at different speed in a Dish/Stirling system [28]

insulation of the receiver or glass covering, and optimization of the geometry and

orientation. The convection losses due to wind can significantly influence the efficiency of the entire system if the wind speed reaches high values. Wind can also cause additional optical losses in the system due to mechanical loads placed on the components and on the structure, causing misalignment and so optical losses. In Figure 2.13, the wind effect is shown on the output electricity of a Dish/Stirling system with a constant Irradiance of 1000 $\frac{W}{m^2}$ [28]. The output power without any wind is 42 kW, whereas if the wind speed reaches 7 $\frac{m}{s}$ the electric power becomes 28 kW, with a reduction of 33%.

Conduction Losses

The thermal losses by conduction can happen between the receiver and the insulating layer, if there's one, and the receiver support which bears the absorber. They represent a minority part of the total losses. They can be expressed for one-dimensional geometry of a homogeneous insulating material of width L and thermal conductivity k as follow [23]:

$$\dot{Q}_{\text{cond}} = kA\frac{(T_{\text{rec}} - T_{\text{amb}})}{L} \tag{2.13}$$

These losses are directly proportional to the temperature difference between the receiver and the ambient and inversely proportional to the thermal resistance of the material.

Total Losses

To consider the total losses of the receiver, one can simply sum together all the previously mentioned loss shares:

$$\dot{Q}_{\text{loss}} = \dot{Q}_{\text{rad}} + \dot{Q}_{\text{conv}} + \dot{Q}_{\text{cond}} \tag{2.14}$$

These are the principal loss sources, but this equation is not comprehensive of other minor ones that can happen. More in general the loss term can be inserted into the instantaneous steady-state energy efficiency of the receiver [23]:

$$\eta_{\text{rec}} = \frac{\dot{Q}_{\text{converted}}}{\dot{Q}_{\text{input}}} = \frac{\dot{Q}_{\text{input}} - \dot{Q}_{\text{tot loss}}}{\dot{Q}_{\text{input}}} \tag{2.15}$$

where the $\dot{Q}_{\text{input}}$ is the total power incident on the receiver due to concentrated solar radiation. It can be evaluated in general by considering factors such as solar irradiance, concentration ratio, receiver aperture area:

$$\dot{Q}_{\text{input}} = I_{\text{in}} \cdot C_r \cdot A_{\text{ap}} \tag{2.16}$$

with $I_{\text{in}}[\frac{W}{m^2}]$, *Solar Irradiance*, being the power per unit area received from the Sun's radiation. The concentration ratio C_r is inserted in the equation, representing the factor by which the incoming solar radiation is concentrated onto the receiver aperture, determining the amount of solar radiation that is actually incident on the receiver.

Chapter 3

Thermal storage

3.1 Introduction to storage

Energy storage systems represent a fundamental component for today's energy infrastructures, playing a major role in various applications, improving reliability, efficiency and security of energy supply and consumption. Furthermore, as seen in Chapter 1, the global electricity demand increase will become a major issue in the near future, so exploiting energy in the most efficient way will be crucial for a smart employment of our resources and outputs. The primary purpose of these systems is to store energy when it is abundant and release it when it is more needed, enabling an efficient capture, storage and utilization. In particular, not having a storage for electrical applications can lead to grid instability, due to the difficulty to always balance supply and demand, exposing the system to voltage and frequency fluctuations, damaging the electric grid and causing power outage. Moreover, the production of electricity from intermittent energy sources (like most of renewable sources) leads to an inefficient energy generation, in addition to the problems mentioned before. For thermal systems, the absence of a storage can lead to thermal overheating if there is not another dissipation source, or lower efficiency due to large amount of wasted energy. In particular, in this thesis the focus will be mainly on thermal storage, which involves lower costs, less space and still has great margin of development. It is also an alternative to the depletion of the most common materials used for the manufacture of batteries, such and lithium and nichel, and doesn't need any critical or potentially polluting operation or disposal. Battery storage systems are more suitable for applications requiring certain characteristics such as fast response times, which are not as important in our system. More in general, some of the main benefits of the thermal storage are [29]:

- **Increase generation capacity**: Thermal energy storage allows energy to be

stored when it is abundant and released when needed. It can also increase the generation capacity of the system during peaks of high demand.

- **Enable better operation of cogeneration plants**: Cogeneration plants produce both electricity and heat simultaneously. However, the demand for electricity and heat may not always align. Thermal energy storage allows excess heat generated during periods of low heat demand to be stored for later use when heat demand is higher. This load balancing capability helps optimize the operation of the cogeneration plant by matching energy production with energy demand more effectively.

- **Shift energy purchases to low cost periods**: With a TES system, excess energy generated during periods of low demand or when energy prices are low can be stored for later use. By purchasing and storing energy when prices are low and using stored energy during periods of high demand or high prices, energy costs can be optimized, leading to potential cost savings for the system operator or end-user.

- **Increase system reliability**: The storage lends the ability to consistently deliver energy to meet the demands of users over time, under various operating conditions, without interruptions or failures. A reliable energy system is one that can maintain a stable and uninterrupted supply of energy, ensuring that consumers have access to the energy they need when they need it.

- **Integration with other functions**: TES systems can facilitate the integration of renewable energy sources such as solar and wind power by storing excess energy for use when renewable energy generation is intermittent or unavailable. They can be useful also with other functions, such as combined heat and power (CHP) systems or district heating and cooling networks

One of the main advantages for the CSP system is that thermal storage can be designed to closely match the temperature requirements of the CSP plant, also for high temperature applications, optimizing energy transfer and efficiency. This enables efficient integration with the CSP plant's power cycle allowing for operations under different solar conditions and final uses like heating, cooling, or power generation.

3.2 Classification of Thermal Energy Storage

Thermal storage systems can be categorized based on the method used to store and release heat energy (Figure 3.1). The main categorization is between physical and chemical processes, different in their underlying mechanisms and outcomes.

The former experiences changes in the physical state or properties of matter without altering its chemical composition. It does not involve the formation of new substances and it is related to reversible changes in temperature, pressure or volume. Processes included in this definition are state changes or changes in size or shape. Instead, chemical processes involve changes in the chemical composition of matter, resulting in the formation of new substances. These processes are characterized by the breaking of chemical bonds in reactant molecules and the formation of new bonds in product molecules. They are typically irreversible and are usually related to changes in the potential energy of chemical bonds and absorption or release of heat or light. The physical processes can then be further divided based on sensible and latent heat. Sensible heat is associated with changes in temperature of a substance without a change in its phase; when absorbing or releasing heat energy, the temperature changes proportionally. Latent heat, on the other hand, is associated with changes in phase of a substance without a change in its temperature. During phase transitions, heat energy is absorbed or released as the substance changes from one phase to another. Unlike sensible heat, which causes changes in temperature, latent heat causes changes in the internal energy of the substance as molecules rearrange during the phase transition. For both processes the original state of the substance can be restored by adding or removing heat energy.

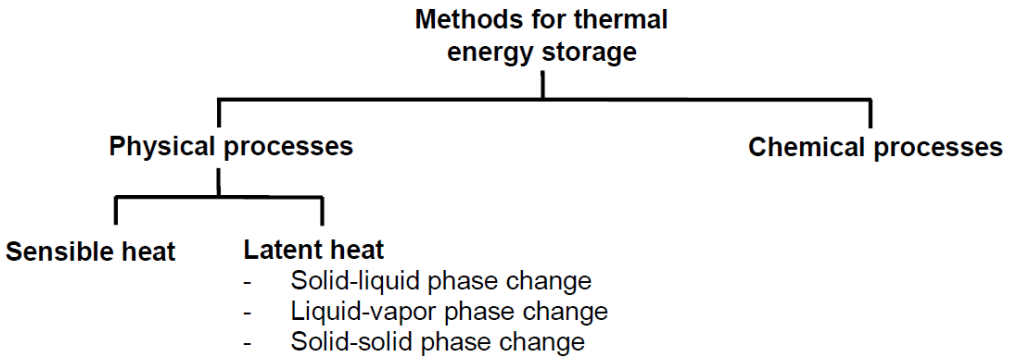

Figure 3.1: Schematic of different thermal energy storage methods [30]

3.2.1 Chemical process

This kind of process involves storing thermal energy through reversible chemical reactions that occur with high heat of reaction (enthalpy difference between the end and the start of the reaction). During the charging phase, the system absorbs heat to drive an endothermic reaction, converting reactants into higher-energy products. The stored energy is then released during the discharging phase, as the system undergoes an exothermic reaction to revert back to its original state. Therefore,

during the exothermic reaction, the heat becomes available for a time shifted use. The equation that quantifies the stored heat is:

$$\Delta Q = \Delta H = m\Delta h \tag{3.1}$$

In Figure 3.2, a schematic of a thermochemical energy storage (TCES) is provided. Charging and discharging cycles are carried out in separate reactors with storage tanks in between for continuous operation. In the initial charging reactor, heat is supplied, making solid component A react with solid component B, releasing water vapour. Following a storage period, component B is transferred to the second reactor, where water is introduced, facilitating the release of stored energy. Eventually the cycle ends restarting the process by transferring component A back to the initial reactor [31]. The materials that could be used in these kind of processes are metal oxides, hydrated Salts and ammonia. The binding energy in a

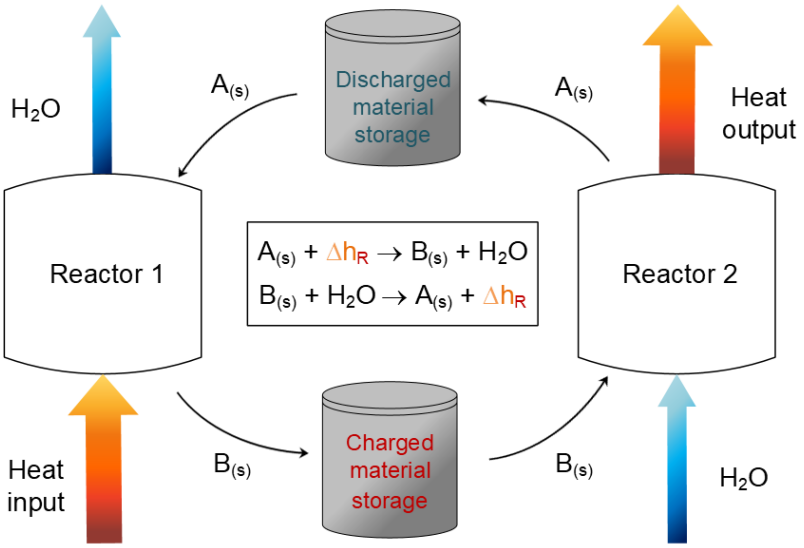

Figure 3.2: Schematic of a Thermochemical Energy Storage [31]

chemical reaction tends to be high, necessitating a significant amount of energy to break it apart and, when solids or liquids are involved, the required storage space is typically minimal [30].

3.2.2 Sensible Heat process

The storing process by sensible heat is connected to the temperature change in the substance. It relies on the heat capacity of a substance ($C[\frac{J}{kg°C}]$), which is the ability to absorb or release heat energy as its temperature changes. The amount of

heat stored can be calculated by the following formula:

$$\Delta Q = C \cdot \Delta T = mc\Delta T \tag{3.2}$$

This kind of storage can be used is various applications, such as water heating systems or space heating in buildings. In Figure 3.3, a simple system for space and domestic water heating is presented, with water as the sensible heat storage medium. The lower cold water layer in the tank is sent to the solar collector, where it is heated and sent back to the upper part of the storage, creating a temperature stratification. In the secondary loop, cold potable water and the one circulating in the radiators gets heated and sent back for the domestic applications. Although it is the most simple storing system, it has the main disadvantage of

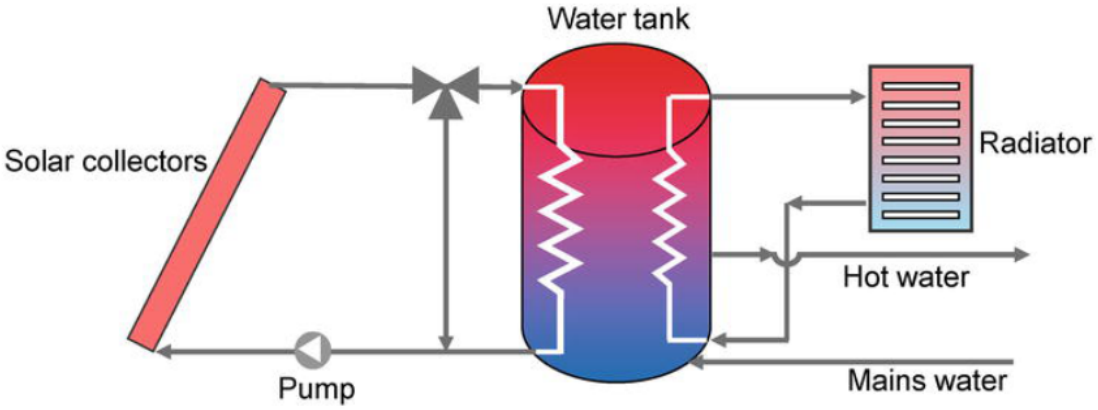

Figure 3.3: Sensible heat application for space and domestic water heating [32]

having a very low energy density compared to others, being a limitation in space constrained applications. Furthermore, the duration of thermal storage is limited and the effectiveness depends on the temperature difference between the charging and discharging phases. In situations where the temperature differential is small, sensible heat storage may be less efficient.

3.2.3 Latent Heat process

Thermal latent heat storage is a method of storing and retrieving thermal energy by exploiting the phase change of a material. During the charging phase, the heat is absorbed by the material ideally at constant temperature, causing it to undergo a phase change to a higher energy state. The process is reversible and the discharge phase is still at constant temperature, but to the initial lower energy state, making it possible to retrieve the energy previously stored. The temperature at which a phase change occurs is called the melting or boiling temperature, depending on the transformation that takes place. Materials that can store and release large

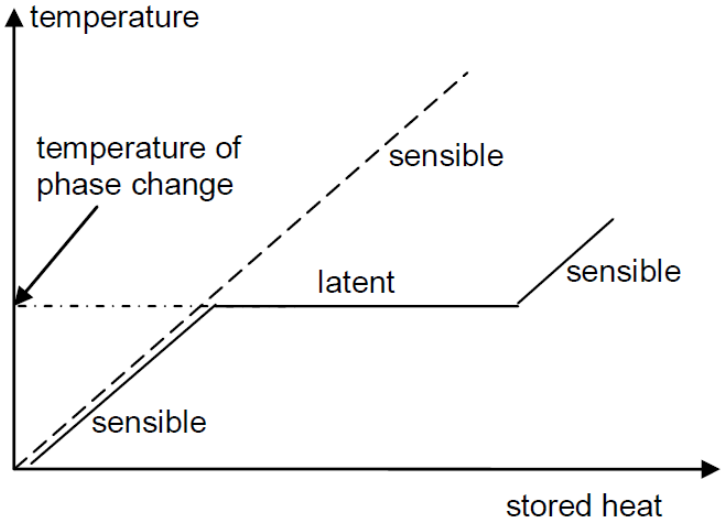

Figure 3.4: Graphic of stored heat for sensible or solid-liquid heat application [30]

amounts of energy during the process of phase transition, typically between solid and liquid states, are called *PCMs*, *phase change materials*. The equation that can evaluate the energy stored in a PCM is the following [33]:

$$\Delta Q = m[c_{\mathrm{p,sol}}(T_{\mathrm{melt}} - T_{\mathrm{sol}}) + \Delta h_{\mathrm{fus}} + c_{\mathrm{p,liq}}(T_{\mathrm{liq}}) - T_{\mathrm{melt}}] \tag{3.3}$$

In the charging phase, the first part accounts for the sensible energy stored from the initial temperature of the solid to the melting one, the second term for the latent heat of fusion, and the third one for the sensible part till the final temperature of the liquid. In case the melting will not be completed, the third term will be deleted and the second decreased. In Figure 3.5, the charging and discharging phases of operation of a PCM are both displayed. The stored heat reaches its peak at the highest temperature of the liquid phase, gradually decreasing to zero as the material is fully discharged. The liquid vapor transformation instead strongly depends on the boundary conditions, not making it feasible for heat storage in some cases. In open systems utilizing water, liquid-vapor phase change is suitable for heat storage due to the ability to freely release and condense water vapor, while closed systems using other substances may encounter challenges related to pressure and volume changes. For what concerns solid-solid phase change, it shows similarities with solid-liquid phase transition, although typically featuring lower phase change enthalpies [30]. The main advantage for PCM storage is high energy density. Phase change transformation involves much larger amount of energy compared to temperature changes, allowing for a higher energy density of the material. Some applications could be solar thermal power plants, district heating systems, and thermal energy storage for buildings. The other main advantage is

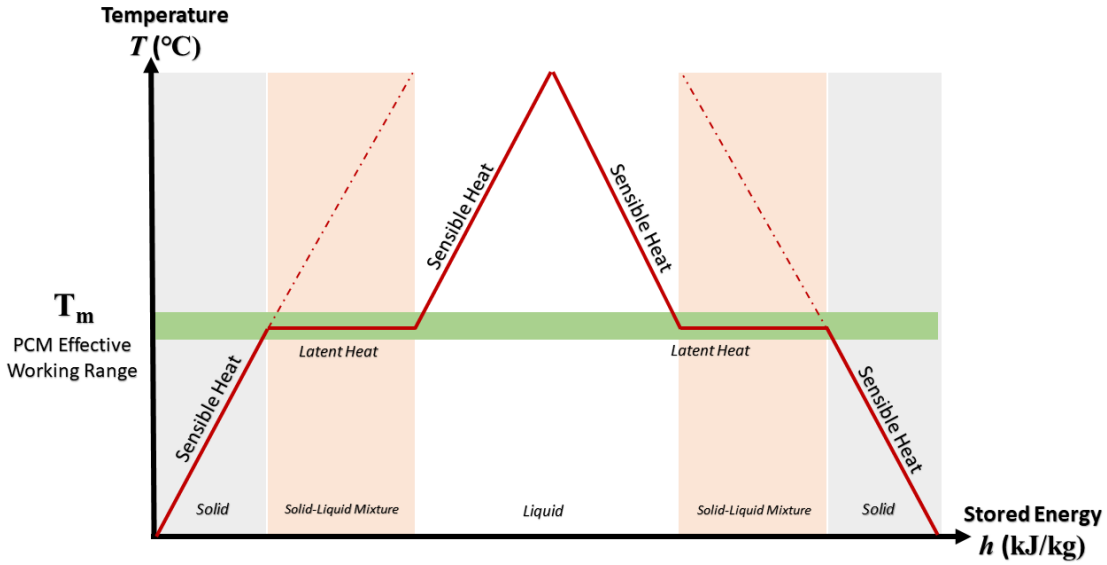

Figure 3.5: Graphic of operation of a PCM [34]

the ability to operate at a specific temperature, allowing to have a good control where temperature fluctuations need to be minimized, such as in thermal comfort systems for buildings. The analysis will now concentrate on PCM, which will be the most suitable storage for the solar application under investigation.

3.3 Phase change materials

In this section only solid-liquid PCM will be considered. The purpose is the selection of suitable phase change material with appropriate melting or boiling points and thermal properties. In addition, the design and operation of latent heat storage systems could require consideration of factors such as heat transfer rates, thermal cycling durability, and compatibility with surrounding components for a complete analysis. The latent heat storage offers a promising solution, with ongoing research and technological advancements, playing an important role in enhancing energy efficiency. The main classification can be done accounting for the chemical composition of different PCMs (Figure 3.6):

- **Organic PCM**: Derived from carbon-based compounds such as paraffins, fatty acids, alcholos, esters. One of the main characteristics is the large temperature range in which they can be synthesized to undergo phase transition (-80°C to 275°C). It allows organic PCMs to be customized for specific application requirements, offering flexibility in thermal energy storage systems. In addition to that, the chemical stability, non corrosiveness and non toxicity permit the

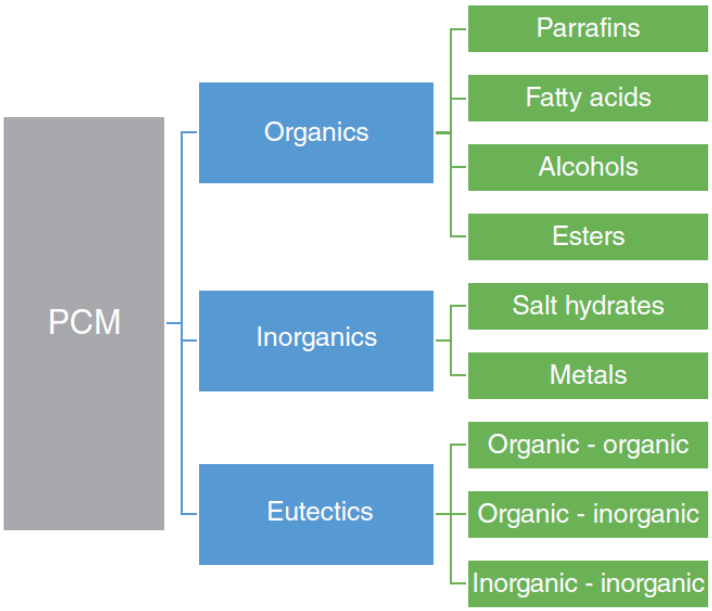

Figure 3.6: PCMs classification by chemical composition [29]

compatibility with a wide range of encapsulation materials. This compatibility facilitates the integration of organic PCMs into thermal energy storage systems, allowing for easy handling, storage, and deployment in practical applications. This kind of PCMs also don't experience supercooling, that is the phenomenon where a substance remains in a liquid state below its normal freezing point or in a solid state above its normal melting point. The main disadvantage is their low thermal conductivity (0.1-0.5 $[\frac{W}{mK}]$), and a significant volume change.

- **Inorganic PCM**: They are typically made up of elements other than carbon, such as metals, or salts. Inorganic PCMs typically have higher melting and freezing points compared to organic materials, making them suitable for applications requiring thermal energy storage at elevated temperatures. The volume change is negligible, and their thermal conductivity surpasses that of organic compounds (0.5-5 $[\frac{W}{mK}]$), enabling a more uniform phase change throughout the material. This property is particularly advantageous for large-scale PCMs, where temperature variations across the distribution may occur. However, the supercooling problem is present, and may not be fully compatible with other encapsulation materials.

- **Eutectic PCM**: Eutectic materials are made from two or more substances, forming a homogeneous mixture, that has a lower melting temperature than any of its individual components. Therefore, the main advantage is the possibility to change the composition of the substances to arrive to an exact melting

point, specific for the application which has to be carried out. Moreover, they usually present a high energy density. The main problem is the limited dataset available, due to the long time requirement for studying various compositions and all the related characteristics.

3.3.1 Selection criteria of the appropriate PCM

Finding the right Phase Change Material for thermal storage involves a balance between multiple characteristics more or less important for specific application requirements. This process often consists of compromises to achieve the optimal solution, favouring one path rather than another. The most important fields of application in which PCM is usually deployed are thermal inertia and storage.

- The biggest limiting factor is that the **phase change temperature** must align closely with the application's operational temperature range. Finding the proper value ensures maximum energy storage and release
- PCM's heat storage capacity, typically measured by its **latent heat of fusion**, is a critical consideration. Higher latent heat values signify greater energy storage capacity per unit mass or volume, which is desirable for applications requiring compact and efficient thermal storage solutions
- The **thermal conductivity** of the PCM is another crucial factor to consider. A high thermal conductivity facilitates rapid heat transfer within the material, ensuring uniform temperature distribution and efficient charging and discharging processes, especially for applications with extended PCM dimensions
- Practical factors such as material **compatibility**, **stability**, and **reliability** over multiple thermal cycles are essential. PCMs should exhibit good chemical stability, minimal degradation, and compatibility with container materials and operating conditions to ensure long-term performance and reliability
- **Economic factors** such as material cost, availability, and scalability, play a significant role in PCM selection. While certain PCMs may offer superior performance characteristics, their widespread adoption may be hindered by cost considerations or limited availability

3.3.2 Methods of PCM integration

The greater attention of PCMs integration is on the **building sector**, due to the large amount of energy waste because of thermal inefficiency and their potential of integration into various construction elements. The utilization of PCMs in this

sector extends to various construction elements such as building materials, envelopes, facades, walls, roofs, floors, windows, and shading equipment, effectively mitigating thermal effects, reducing energy consumption, and decreasing the building sector's emissions footprint [35]. They could also be used in clothing, for thermal regulation, refrigeration cycles, food preservation and medical applications. Regarding the solar field, it was decided to delve into the encapsulation of PCMs to facilitate their management when utilized alongside heat transfer fluids. This approach aims to separate the phase change materials from the heat transfer fluid by encapsulation, allowing for proper use through the following factors [36]:

- Fulfilling the requirements for strength, flexibility, corrosion resistance, and thermal stability
- Controlling the release rate of the PCM for a specific requirement and minimizing leakages
- Serving as a barrier to shield the PCM from adverse interactions with external factors such as moisture, oxidation, and chemical reactions, which can degrade the performance over time. This helps maintain the PCM's properties and stability during storage and application.
- Offering wide surface area for efficient heat transfer with the fluid which has to retrieve the stored heat
- Providing structural stability, ease of handling and versatility for a wide range of applications

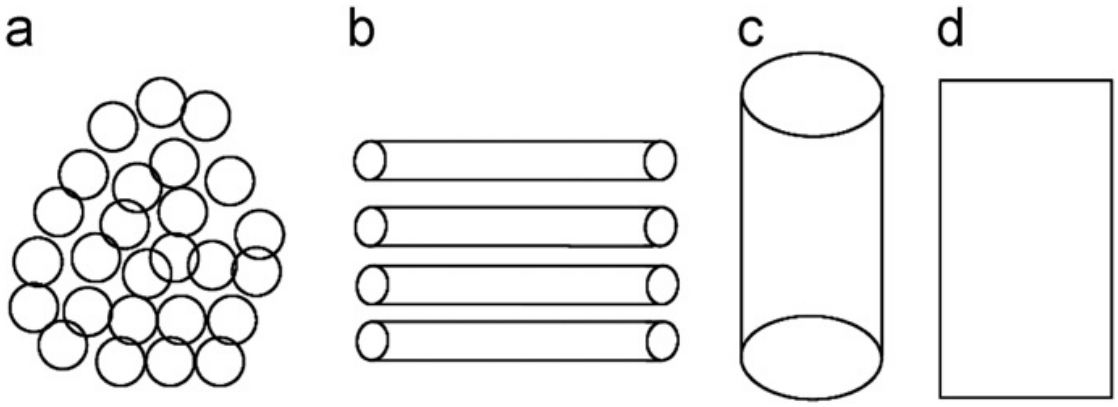

Figure 3.7: Different PCMs encapsulation geometries, (a) Spherical, (b) Tubular (c) Cylindrical (d) Rectangular [37]

In Figure 3.7, the most common encapsulation geometries are shown. Various encapsulation techniques are employed based on the specific requirements of the

application. Each technique offers unique advantages in terms of scalability, cost-effectiveness, and performance. The major distinction can be made with:

- **Macroencapsulation**: It involves encapsulating the PCM within a relatively large container or structure, from more than 1 millimeter to several meters. The main advantage is the easy fabrication and handling, making it suitable from small to large scale applications
- **Microencapsulation**: It involves enclosing PCM particles or droplets within microcapsules, typically ranging in size from a few micrometers to 1 millimeter. These microcapsules are then dispersed within a matrix material, such as a polymer, to form a composite material with enhanced thermal properties. This technique is commonly used in applications requiring precise thermal control. The main problem could be related to the thermal conductivity of the matrix, whose rigidity can also hinder convective currents and force the transfer by conduction. In addition, until today the cost of fabrication is still high [36].

Given these different characteristics, the technique of macroencapsulation is chosen for solar applications due to its ease of operation, manufacturing, and cost. In Figure 3.8, a simple charging-discharging schematic of the encapsulation is displayed, with an inner PCM droplet or particles layer and a polymeric or metal external shell. If volumetric expansion of the inner material is significant, a gap filled with a gas, commonly air, is present to prevent internal mechanical stresses. The most

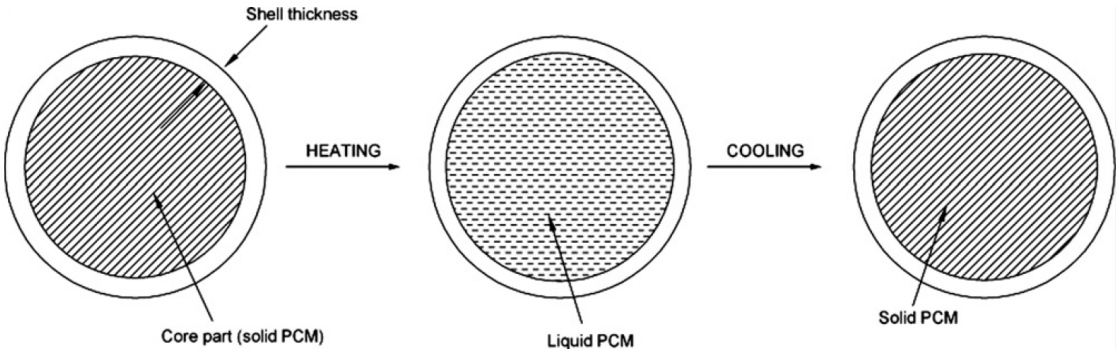

Figure 3.8: Simplified schematic of the structure of an encapsulated PCM during charging and discharging phases [37]

important parameter for the correct encapsulation is the *Core-to-Coating Ratio* (the volume ratio between the PCM and the shell), is it too high the coating would not be appropriate for mechanical endurance, whereas a low ratio will decrease the PCM inside and so the storage capacity. More in general, the introduction of silver nanoparticles could enhance thermal and structural stability [37]. The thermal

conductivity is another crucial factor. To compensate for the low conductivity of organic PCMs, inorganic shell materials are preferred, particularly silica, which has demonstrated suitable thermal properties. More in general, to reach high thermal transfer rates, metallic materials like copper, aluminium or steel are preferred [37]. In Figure 3.9, various macroencapsulation systems in a HTF stream are shown.

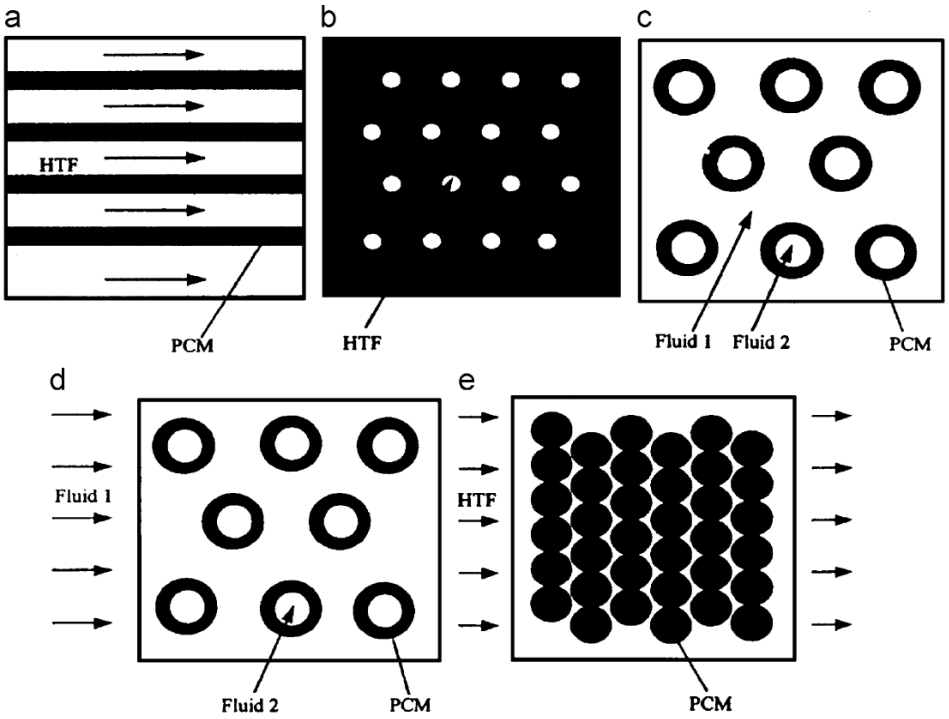

Figure 3.9: Different PCMs macroencapsulation systems, (a) Flat-plate or Cylinders, (b) Shell-and-tube with Internal flow, (c) Shell and-tube with parallel flow, (d) Shell-and-tube with cross flow, (e) Sphere packed bed [38]

The geometry and arrangement of encapsulated PCM within a heat transfer fluid can vary significantly depending on the specific system requirements and design considerations. Various factors, such as the intended application, thermal performance objectives, and practical constraints, influence the choice of PCM geometry and disposition. Flat-plate or cylinders are suitable for applications where the main goal is a uniform heat distribution, whereas shell-and-tube with internal flow enables precise control over the flow rate and temperature of the heat transfer fluid. Shell-and-tube with parallel flow has a good heat transfer efficiency by maximizing the surface area of contact between the PCM and the heat transfer fluid, further improved in shell-and-tube with cross flow by promoting turbulence of the fluid. Sphere packed bed can maximize the surface area available for heat exchange. The final choice for the material will be made afterwards, mainly

depending on the operating characteristics of the experimental tests, to pair them with the characteristics of the storage system.

Chapter 4

Case Study

4.1 Energy Center Solar Collector

For our case study, we will analyze the parabolic solar concentrator located on the roof of the Energy Center in Turin. The concentrator costed around 18000 € and

Figure 4.1: Solar parabolic dish on the Energy Center

it was installed in 2019 by *Electronic Machining Srl.*, a company specialized in industrial automation solutions. The installation was undertaken for the purpose of conducting laboratory experiments for research and temporary use. The parabolic dish is shown in Figure 4.1; its concentration part is made of aluminium coated with reflecting polymer strips placed in the concave part of the structure. These thin films taper to the centre covering the parabola, except for the central point, which lacks a reflecting surface due to the presence of a metal arm which supports the receiver structure where the focal point is concentrated. Have to pay attention to the reflective strips during maintenance to prevent the formation of air bubbles, which could make the surface uneven, affecting the focal point's position at certain times of the day. It is also present a dual-axis tracking system, controlling azimuth

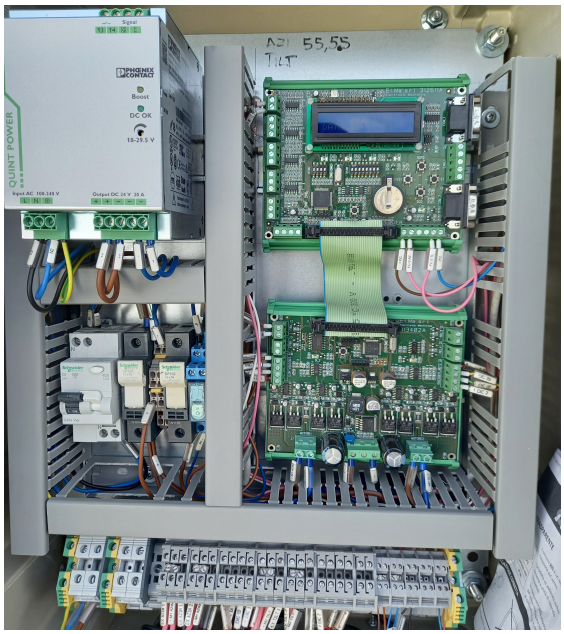

Figure 4.2: Control Unit of the Parabolic Dish

and tilt angle and guided by a control unit (Figure 4.2) which allows for optimal exposure to solar radiation. The tracking direction is calculated in real time, taking into account the date, time, latitude, and longitude, ensuring an accuracy greater than 0.015°. There are two aluminum joints that, when overlapped, indicate the initial zero position of the parabolic movement [39]. The concentrator presents the construction features reported in Table 4.1. There is also a control cabinet connected to the receiver by pipes carrying heat transfer fluid. Two tanks of CH_4 and Argon are present for different thermal fluids, through which the flow rate of the circulating gas can be controlled by pumps and temperature measured. The former can be used for chemical looping reforming (CLR) to produce hydrogen, whereas

the latter is considered useful for its inertness and stability at high temperatures.

Characteristic of the Solar Dish	
Collecting Surface	4.5 m^2
Average Direct Radiation	800 W/m^2
Max Temperature at the focal point	1800°C
Concentrated Power, Optimal Conditions	2.8 kW
Optical Efficiency	80%

Table 4.1: Production Characteristics of the collector [39]

4.2 Tests with different receivers

4.2.1 Alumina Receiver

The receiver should have certain characteristics to effectively capture and utilize concentrated solar energy, among which:

Figure 4.3: Alumina cylinder positioned at the focal point

- High temperature resistance
- Efficient heat transfer and absorption properties

- Minimal heat loss
- Compatibility with heat transfer fluid
- Durability

In particular, alumina, Al_2O_3, has been chosen for the system due to its ease of construction, as well as its high melting point (over 2000°C), chemical resistance to corrosion, and good solar absorption, although thermal conductivity is not so high. A hollow cylinder made of alumina (Figure 4.3) was manufactured, measuring 22 cm in length, with an outer diameter of approximately 1.8 cm and an internal of 1.4 cm. The cylinder is positioned at the focal point and secured by two forks,

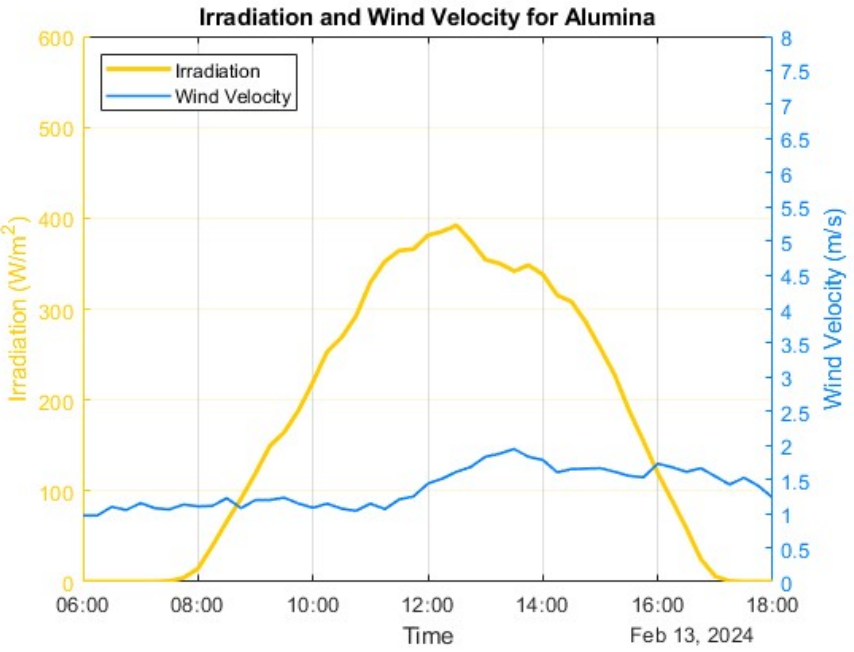

Figure 4.4: Average Irradiation and Wind Velocity during the Alumina tests

with a heat exchange fluid passing inside. To measure the temperature, a Type N thermocouple is employed, providing accurate readings for temperatures above 100°C, although it is less effective for lower temperature ranges. It is made of of nickel-chromium (NiCr) and nickel-aluminum (NiAl) alloy wires, providing chemical stability and a reliable performance over time. Despite the structural fragilities observed in alumina during previous tests, there was a decision to revisit and repeat those tests in order to validate the results of earlier experiments. These tests were carried out either concurrently with or subsequent to the materials that will be presented afterwards, but they will be discussed first to maintain a conceptual order

in reporting. The measurements were performed with the thermocouple inserted inside the cylinder in contact with the wall closest to the solar concentration, during the period from November 10th to November 26th, 2023. In addition to this, meteorological data were collected for the specified time frame, with recordings taken every 15 minutes. Subsequently, an average Irradiation (W/m^2) by each time slot of the same period was computed, as shown in Figure 4.4. In November, the irradiation values may not be notably high, as this month typically sees reduced solar radiation levels due to factors such as shorter daylight hours and potential cloud cover. The detection of radiation typically starts around 8:00 and ceases around 17:00 and the highest value reached in those days was 392 W/m^2. The

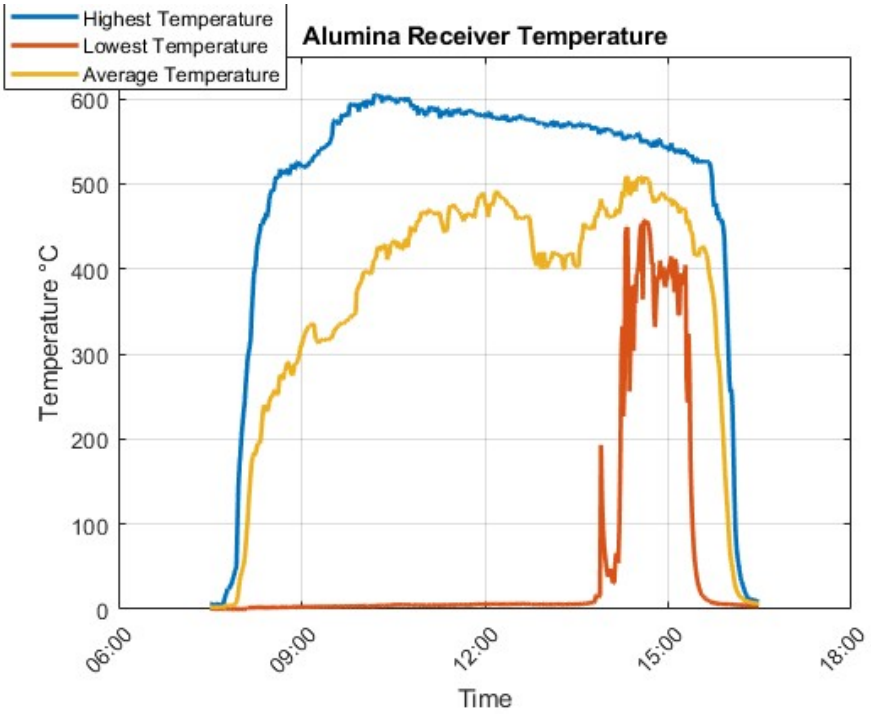

Figure 4.5: Highest, lowest and medium temperature for Alumina for each recorded time

Graphic 4.5 displays the maximum, minimum, and average temperature for each measurement of the alumina receiver. The highest recorded temperature reaches around 600°C, occurring between 10:00 and 10:30. The intensity of sunlight peaks around mid-morning, at 12:00, but the highest values recorded for alumina are before this time frame. This shift occurs because, as the day progresses, other factors such as wind convective cooling may start to counteract the heating effects of sunlight, preventing the receiver from reaching higher temperatures later in the day. The minimum temperature for each recorded time tends to reach values close

to zero because there have been some measurements taken in cloudy weather. In Figure 4.6, notice the large variability in temperature based on the atmospheric conditions of the day when the tests were conducted. On the left, a very cloudy day resulted in a significant temperature variability, while on the right, the clear sky day allowed for a uniform receiver temperature. But as previous tests have

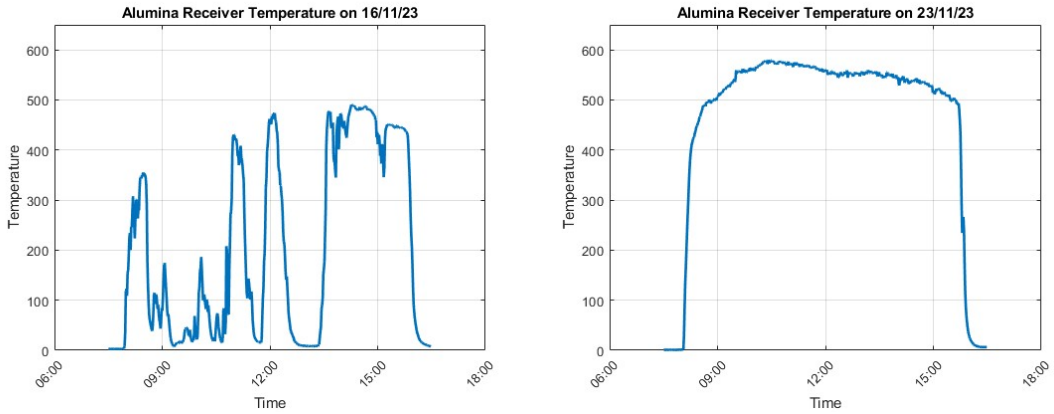

Figure 4.6: Comparison of the Alumina Receiver in a cloudy and clear sky

shown, alumina has proven to be unsuitable for high cyclic thermal stress and high temperature gradients. Within just ten days, signs of darkening were evident along on the edges. Depending on the conditions and specific reactions occurring, the properties of the alumina, such as its crystal structure, purity, and surface characteristics, may be altered, resulting in observable changes such as darkening or discoloration. And after another 7 days, the receiver experienced a brittle fracture (Figure 4.7), approximately halfway along its length. Alumina, being a

Figure 4.7: The fracture reported in the Alumina Receiver

ceramic material, is inherently brittle, making it susceptible to mechanical failure

in applications where thermal cycling is involved, mailny due to thermal expansion mismatch. This behaviour could be minimized by a more expensive manufacturing, trying to decrease defects or imperfections in the alumina crystal structure, that could promote the nucleation and propagation of cracks, leading to brittle fracture.

4.2.2 SiC Materials

Alternative materials to experiment with were provided by the Department of Applied Science and Technology (DISAT). In this case Non-oxide ceramic matrix composites (CMCs) were chosen, being high-performance materials that have proven effective in challenging environments, such as elevated temperatures and corrosive conditions [40] [41]. In addition to this, the basic properties of ceramics remain, meeting thermal requirements such as temperature range and heat transfer properties, and provide enhanced mechanical properties, such as higher bending and compressive strength. Among the ceramic materials, silicon carbide (SiC)-based ceramics offer good thermal properties, and its high thermal conductivity ensures efficient heat transfer. The most important requirements considered in the fabrication of the receiver [42]:

- "Thermophysical and optical requirements (absorption, heat transfer surface, high fluxes and radial heat transport);
- Material requirements (high porosity, high cell density, thermal conductivity, high thermal shock resistance, high melting point, longer material lifetime, and stability at high temperatures)"

Figure 4.8: Two SiC materials provided by DISAT

The bonding agent to join SiC CMCs, is Yttrium aluminum silicate (YAS) crystals embedded within a glassy matrix. The Yas properties include elevated electrical resistivity, robust chemical durability and stability, diminished thermal conductivity, and a reduced coefficient of thermal expansion, as well as elevated glass transition temperatures, hardness, and elastic modulus [43] [44]. These properties align closely with those of SiC/SiC ceramic matrix composites (CMCs), thereby mitigating thermal stresses within the joint. Such distinctive qualities position YAS systems as highly promising coatings and joining materials for SiC/SiC composites useful for high-temperature applications [45]. The SiC/SiC components were supplied by two different companies, ATL Archer Technicoat Ltd, United Kingdom, and Keraman® SiC/SiC, by BJS Composites GmbH, Germany. The ATL-SiC/SiC composite, provided by ATL, featured first-generation ceramic-grade Nicalon SiC fibers, an interphase coating of boron nitride, and a SiC matrix applied via Chemical Vapor Infiltration (CVI). Instead, the BJS-SiC/SiC composite, provided by BJS, was fabricated using the CVI process with UBE Tyranno® S fibers and an external fiber coating of pyrolytic carbon [43]. The given data are related to Coefficient of Thermal Expansion (CTE), which is important to mitigate the risk of thermal fatigue and extend the operational lifespan of the receiver in case of uneven temperature change in the body, and maintain its shape and alignment. As can be seen from the

Materials	**Reference Temperature**	**CTE** ($10^{-6}{\cdot}°C^{-1}$)
Alumina	(25°C – 600°C)	$7.5 - 8.2$
BJS SiC	(200°C – 600°C)	5.4
ATL SiC	(200°C – 600°C)	5.2

Table 4.2: Different values of CTE for the receiver materials [43]

Table 4.2, the CTE values of SiC compounds are lower compared to those of alumina. This should ensure high resistance to thermal fatigue and extend service operations, reducing the likelihood of structural damage or failure over time. Tests were therefore carried out with the two proposed materials to experimentally verify their thermal qualities as well.

4.2.3 BJS SiC Receiver (White)

Tests for the BJS material were carried out between November 3rd and 8th. Ideally, a cylindrical shape would have been preferred to facilitate a more precise comparison with the data obtained for alumina. However, lacking a cylindrical sample and considering that the thickness of the alumina cylinder is comparable to that of the sample and the temperature measurement is point-like, the data can be directly compared. To ensure accurate readings, the thermocouple was strategically placed

at the rear of the sample to prevent any interference with the focal area (Figure 4.9). The data for the receiver's point-like temperature and atmospheric data for the

Figure 4.9: The white BJS SiC Receiver with the positioned Termoucouple

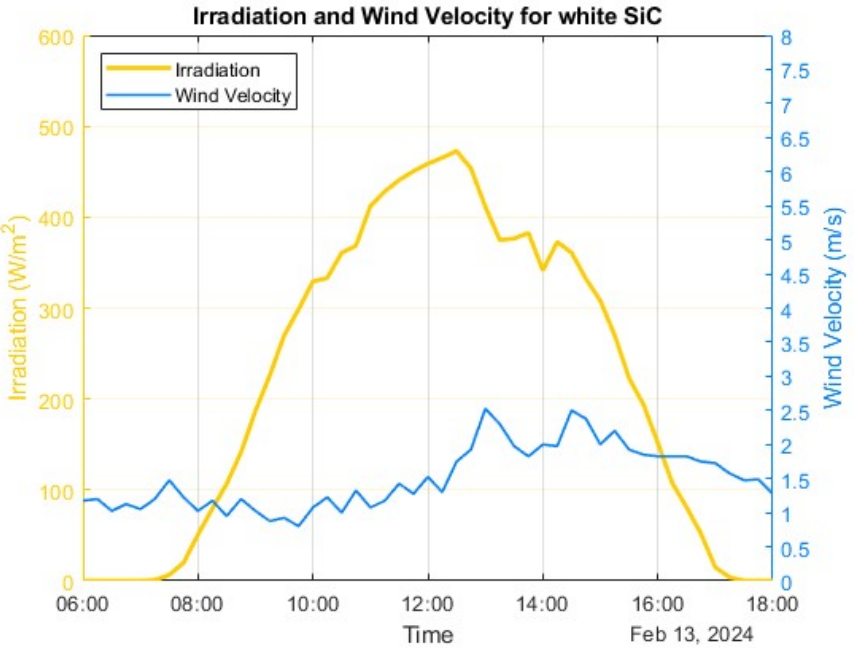

Figure 4.10: Average Irradiation and Wind Velocity during white SiC test

test days were collected. The most relevant atmospheric data, the Irradiation and Wind Velocity, are reported in Figure 4.10. Since the tests were conducted at the beginning of November, prior to those of alumina, solar radiation appears to reach higher values compared to the previous case. Irradiation shows a very uniform curve in the beginning, then from around 12:30 to 14:00, it decreases significantly due to predominantly cloudy conditions on November 7th. The wind remains within a range of average values similar to the previous ones. The Graph 4.11 of

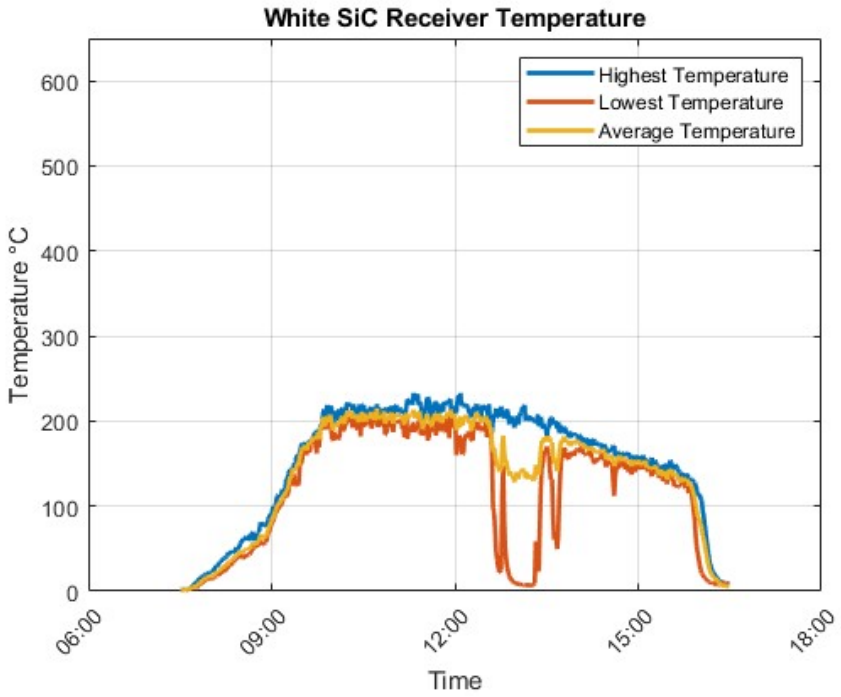

Figure 4.11: Highest, lowest and medium temperature for white SiC for each recorded time

receiver temperatures during the test days is consistent with the recorded solar radiation, showing a very low minimum temperature only during the previously discussed cloudy period. Overall, the average temperature is quite uniform, but the temperature values attained are not satisfactory, as they are around 200 W/m^2, whereas the values for alumina during peak radiation hours almost reached 600 W/m^2. The main problem is related to the receiver colour. Although white surfaces have the advantage of a lower emissivity (and so lower radiative losses of the receiver), the main negative effect is related to the low absorptivity and the higher reflectivity across the solar spectrum. This results in a lower energy absorbed, temperature reached and heat transferred. Although in some solar application it could be useful to prevent overheating or excessive temperature fluctuations, in our

case the receiver will be paired with PCMs, allowing for a proper heat absorption and temperature control. Moreover, a higher temperature is needed for a more efficient energy conversion. So, after the initial tests on the white material, despite appropriate solar radiation, the results were unsatisfactory, and the tests were halted to proceed with the black material.

4.2.4 ATL SiC Receiver (Black)

The analysis now shifts to the second receiver material, which has mechanical properties similar to the previous one but is expected to yield better results due to its color. A basic black material has higher absorption and lower reflection, enabling it to obtain higher temperatures. The tests were conducted intermittently from late October to the beginning of December (Figure 4.12). The irradiation

Figure 4.12: The black ATL SiC Receiver with the positioned Termoucouple

curve (Figure 4.13) is similar to the one for the white SiC, reaching almost 450 W/m^2, whereas the wind curve is comparable in the morning, and starts lining up to higher values right before noon. Therefore, since the average atmospheric values are similar, we can proceed to comparing them to the receiver temperature. As expected, it's possible to reach higher temperatures with the ATL SiC material compared to BJS, as shown in 4.14. The maximum temperatures for each time period range from the peak of solar radiation between 450°C and 525°C. Instead, the average temperature between 10:00 and 15:30 is between 300°C and 425°C. The lowest temperature recorded, as usual, depends greatly on the presence of cloudy days during the tests. The temperature reached seems adequate in this case exhibiting significantly higher temperatures compared to the white one, making it suitable for applications where higher thermal storage temperatures are required, and higher latent heat of phase change and storing capacity. This is because the energy required to change the phase of the material from solid to liquid (and vice

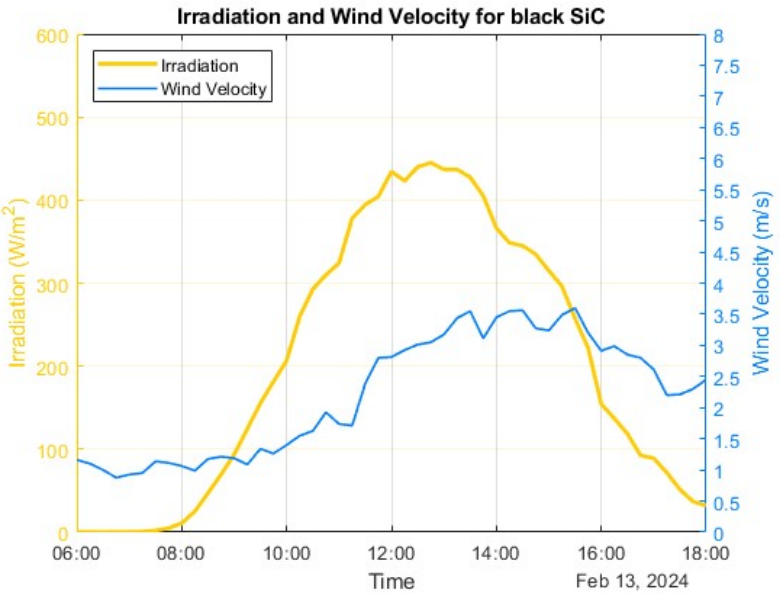

Figure 4.13: Average Irradiation and Wind Velocity during black SiC test

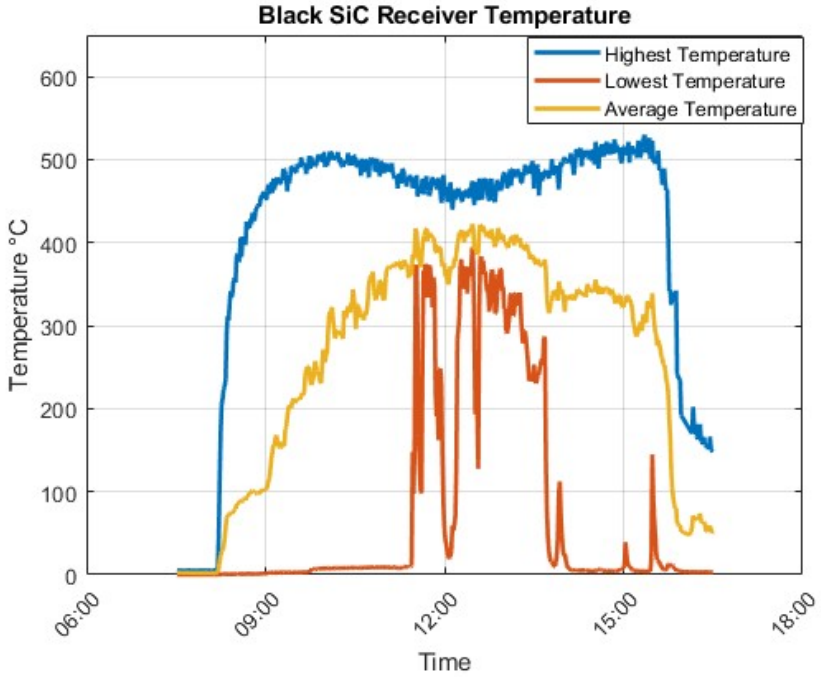

Figure 4.14: Highest, lowest and medium temperature for black SiC for each recorded time

versa) is directly related to the specific characteristics of the material, including its molecular structure and bonding. Materials with higher melting temperatures typically have stronger bonds between their molecules, requiring more energy to break these bonds and transition into a different phase. It wasn't possible to obtain phase change materials for experimental measurements, hence a modeling will be conducted on COMSOL Multiphysics. The modeling process will involve simulating the power deposited on the receiver, the heat transfer and phase change behavior of the PCM within the thermal storage system to optimize its performance and ensure efficient energy storage.

Chapter 5

Modeling of the solar concentration system

In the beginning, the model will primarily concentrate on the dish system and receiver. Following validation with experimental data, it will then serve as the foundation for analyzing the integration of PCM to construct a thermal storage system.

5.1 Modeling of the Parabolic Dish

The parabolic dish will be built on COMSOL Multiphysics with the *Ray Tracing physics*, a computational module used to simulate the behaviour of reflected light rays in a system. For the solar collector it was chosen the paraboloidal reflector shell in the 3D mirrors library. In Figure 5.1 are present some geometrical parameters,

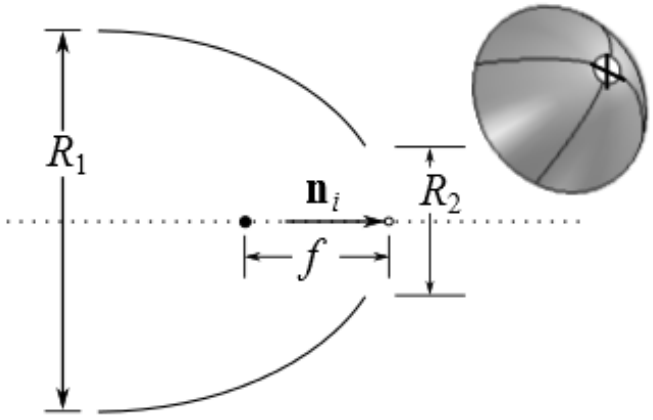

Figure 5.1: Geometrical parameters of the 3d parabolic shell [46]

such as the focal length, that in the Energy Center collector is $f = 0.92\ m$, and the dish radius R_1, that can be expressed as:

$$R_1 = 2f\,(csc(\phi) - cot(\phi)) \tag{5.1}$$

The radius R_2 is this specific case is equal to $R_2 = 0.12\ m$, representing the central part not covered in reflective material, hosting the central metal support arm for the receiver. Therefore the central part will not be taken into account for the ray tracing investigation. The dish projected surface area, which is the projection of the curved object onto a flat surface in a front view, is as a consequence:

$$A = \pi R_1^2 \tag{5.2}$$

Another important parameter for the geometry definition is the rim angle, that for the considered solar collector is $\phi = 0.9028\ rad$. The following effects will be considered in the model to properly characterize the real collector:

- **Roughness**: A real mirror isn't perfectly smooth like an ideal one, there are always slight deviations in the surface that affect the direction of reflected sunlight. Consequently, the focused solar radiation isn't perfectly concentrated, leading to a dispersion of the heat flux over a wider area in the focal plane of the receiver [47]. The surface roughness can be modeled including a *Surface slope error* σ_ϕ, which is an angular error in radiants

- **Absorption**: The absorption coefficient of an ideal mirror tends towards the zero value. For the case reflector the value will of course be higher then the ideal one, with the polymeric film being at high optical efficiency, and an absorption coefficient of $\alpha = 0.2$ (80% of incoming radiation is reflected). Over time there is a degradation of the coating due to exposure to environmental factors and so a reduction in reflectivity. Another worsening factor could be the deposition of materials such dust or impurities. They were not taken into account since the polymeric layer was replaced since not long ago

- **Finite Solar Diameter**: The sun is not a punctual radiation source observed from the Earth, but has an angular extent determined by its finite diameter. This angular size undergoes variations due to the orbits and axial tilts. As a consequence, solar rays entering the system are not parallel resulting in broader focal spots. It can be set up under the angular perturbation section in the software

- **Solar Limb Darkening**: At the center of the solar disk, solar brightness (and so intensity) is at its highest, gradually decreasing as the observer moves towards the periphery or outer edge of the disk. A temperature variation is present within the solar atmosphere. The Sun's atmosphere consists of layers

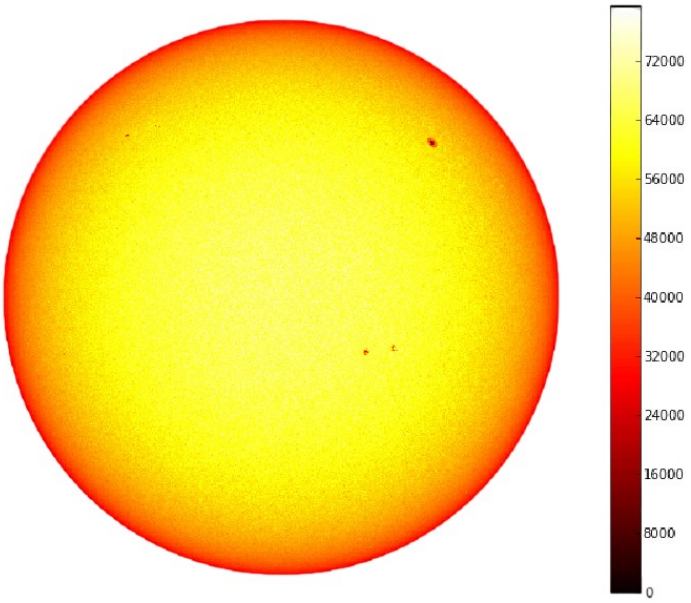

Figure 5.2: Solar photosphere displaying the limb darkening [48]

with varying temperatures, with the inner layers being hotter and the outer layers cooler. In the Sun's center, an observer sees deeper into its atmosphere, where the temperatures are higher because of the intense heat generated by nuclear fusion in the core. Consequently, these deeper layers emit more light, resulting in a brighter appearance. However, when observing towards the limb of the solar disk, the observer's line of sight passes through the outer, cooler layers of the solar atmosphere. These cooler layers emit less light compared to the deeper, warmer layers [49]. Therefore the limb darkening model accounts for a reduction of the reflected radiation from the centre to the edges of the dish. The employed empirical power law for limb darkening is represented by the equation [50]:

$$\frac{I(\psi_s)}{I(0)} = \cos(\psi_s)^{\alpha(\lambda_0)} \tag{5.3}$$

In which $I(0)$ is a the radiation line of the sun's center and ψ_s the angle from the center to another point. The variable α can go from 0, with all uniform spatial radiation, to 1, decreasing linearly in the radial axis moving away from the centre.

5.2 Modeling of the Receiver

The receiver was then characterized as closely as possible to the dimensions of the real alumina one, by building a hollow cylinder with an outer radius of 9.03 mm, an inner of 7.01 mm and a height of 22 cm. The focal plane was identified by the two domains (half cylinder in length) which are exposed to the solar dish. The receiver will be placed exactly at the centre of the focal point, at a distance of 11 cm from the edges. In this preliminary analysis the focus will be only on the deposited irradiation power on the receiver, later investigation will be carried out for heat transfer fluid and phase change material integration, as well as ambient factors like wind convection. In Figure 5.3 all the built system is shown. For what concerns

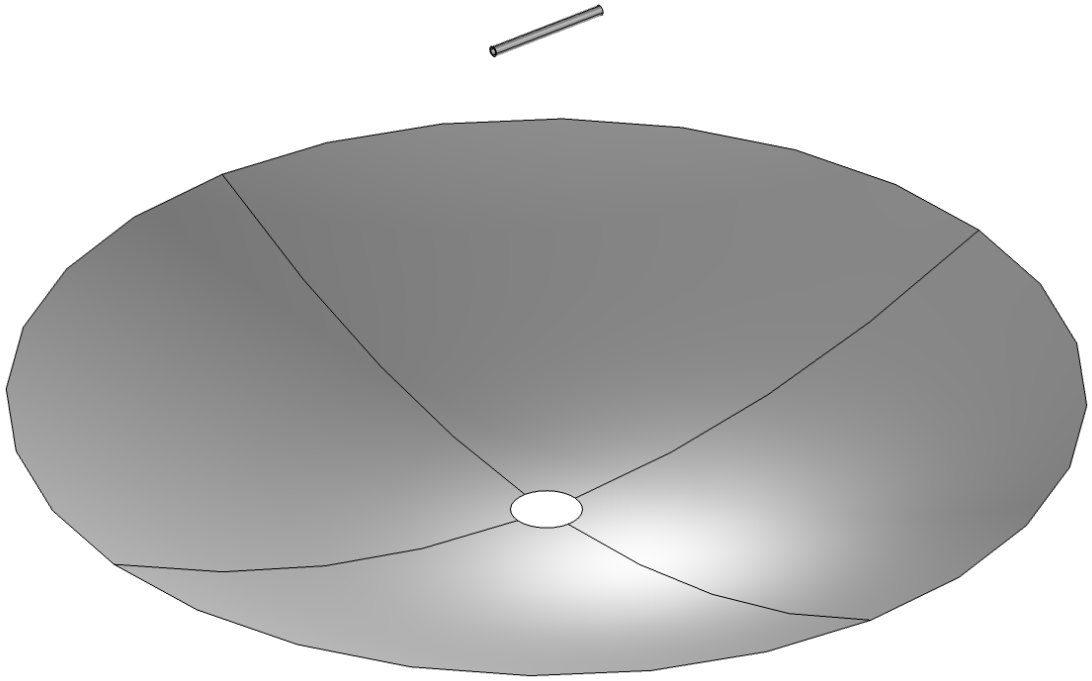

Figure 5.3: Model of the dish receiver system

the mesh, it was chosen a free triangular type. Although it might be not the most accurate mesh, it provides a greater flexibility for adapting the curved surfaces of the collector and the receiver. For the receiver it was chosen the finest mesh due to the importance of correctly evaluating the effect of a large number of rays onto a small surface. The data shown will be relative to the peak irradiation for the average of the month of November, $I = 445\ \frac{W}{m^2}$. In Figure 5.4 it is displayed all the reflected rays power in a spatial distribution of 1.5 m length. In the model the roughness, absorption, finite solar diameter and solar limb darkening are accounted.

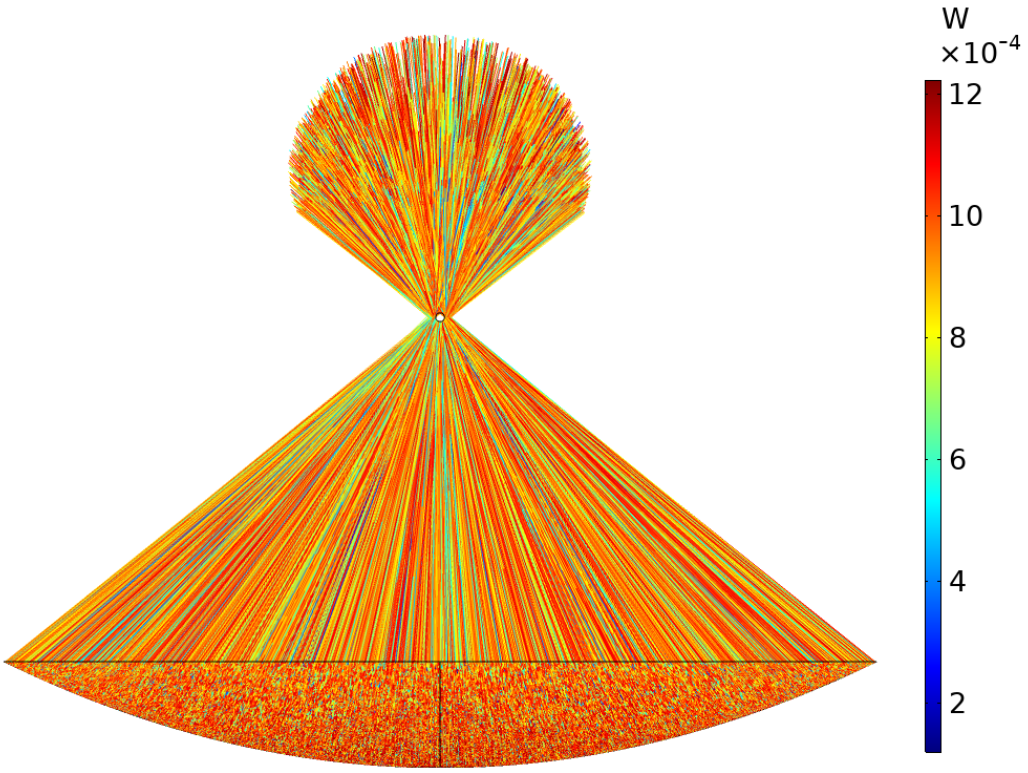

Figure 5.4: Real Ray trajectories power on the receiver

In an ideal case the rays should only intercept the focal plane without surpassing it and should have a more uniform power distribution, from the the higher intensity in the center and then downgrading to the borders. In Figure 5.5, it is present the 3D visualization of the face of the cylinder where the focal plane is located. The power distribution on the receiver is not ideal, meaning that the rays have not been concentrated at a precise theoretical focal point, but rather in a considerably extended area. Within this area, various power regions can be identified. The central red region ranges between $135 - 185$ $\frac{kW}{m^2}$, the yellow-blueish region falls within the range of $60 - 135$ $\frac{kW}{m^2}$, and the outermost region is a more intense blue that degrades to lower values. Obviously, when one moves away sufficiently from these focal areas, the deposited power becomes zero. Because of the difficulty to account for everything in one model, these areas of deposited power will then be exported to another one that will consider other losses at the receiver and thermal evolution within the material. As for the receiver material, the analysis will focus only on ATL SiC, as it was the best material who could show both good structural and thermal characteristics, that are fundamental for a PCM integration.

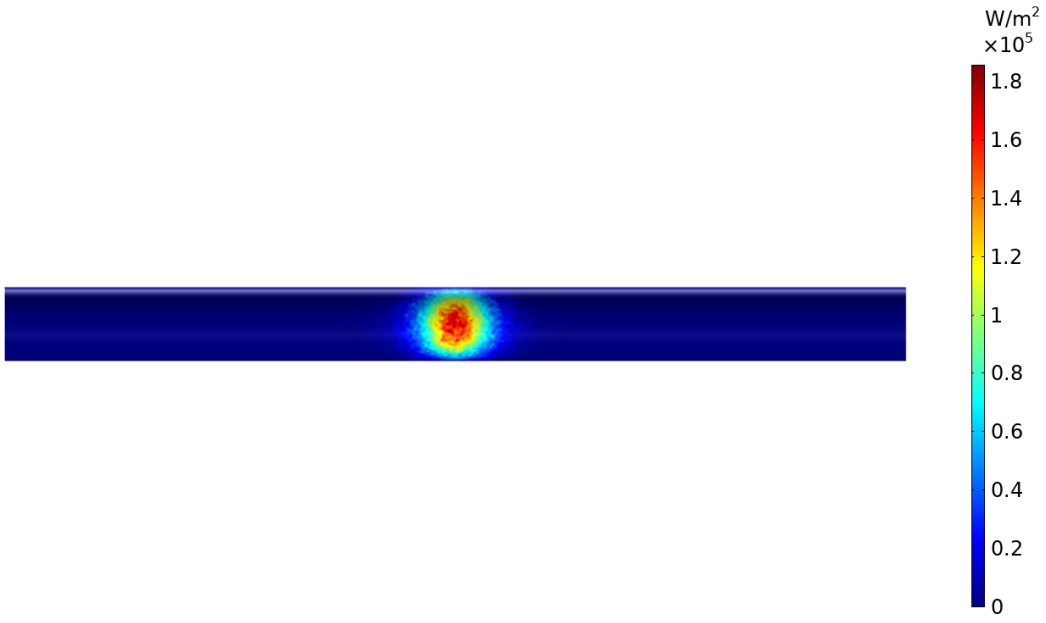

Figure 5.5: Deposited power on the receiver accounting for roughness, absorption, finite solar diameter, solar limb darkening

5.2.1 Receiver thermal dispersion model

The deposited power on the was then modeled onto the receiver focal surface dividing it in the three main areas mentioned before. Every domain was considered with an average value of the deposited power in that area. As it can be seen in Figure 5.6, the power deposited per area in the thermal dispersion model effectively approximates that deposited on the receiver in the optical model. To model the **conduction part** inside the body, the material was firstly initialized as a SiC material in the COMSOL library, and then the most appropriate characteristics for the experimental material were modified. Since the tests will be carried out in the range of significative solar irradiance in November, from 8:00 to 16:00, the initial temperature is set to 5°C as the usual temperature for the initial time of the range. The conduction driving equation for the solid part comes from the *General Equation of Heat Transfer*:

$$\rho c_p \frac{\partial T}{\partial t} + \rho c_p u \nabla T - k \nabla^2 T = 0 \tag{5.4}$$

in which the term $\rho c_p u \nabla T$ is equal to zero due to the absence of translational motion in the model, u. Regarding the thermal dispersion of the receiver, the fundamental contribution to consider is the **wind convection** over the surface.

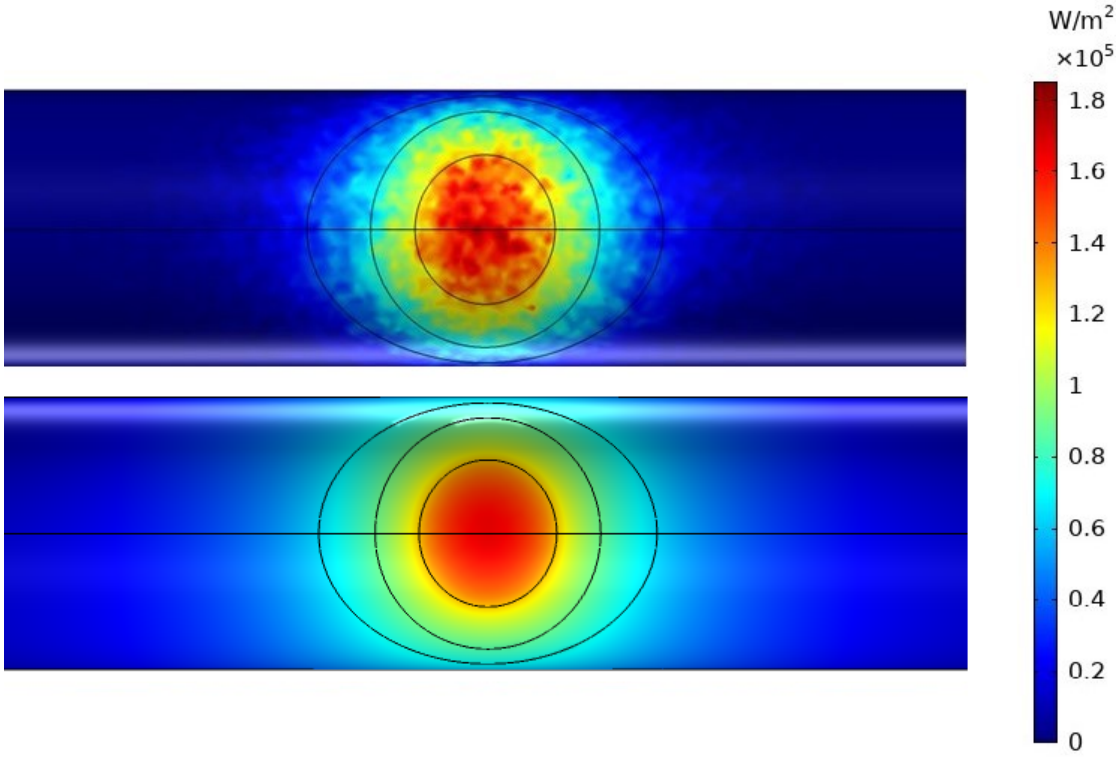

Figure 5.6: Surface division per deposited power in $\frac{W}{m^2}$, the optic model above and the thermal dispersion, without additional losses, below

Wind intensity and irradiance data were collected for all test days and used for the model. As for modeling wind convection on COMSOL, the convective transfer equation is used, that is the Newton law:

$$\dot{Q}_{\text{conv}} = h(T_{\text{rec}} - T_{\text{wind}}) \tag{5.5}$$

The h factor is the *Heat transfer coefficient* in $\frac{W}{m^2 K}$, a measure of the thermal conductivity, that depends on the characteristics of the convection process. An empirical model will be used, that is a simplified mathematical relationship for the complex heat transfer process. In our case, a forced external convection on the outer walls of the receiver was assumed, that is a cylinder in cross-flow (Figure 5.7). The associated empirical model can be expressed as:

$$h = \frac{k}{D}\left(0.3 + \frac{0.62 \cdot \text{Re}_D^{1/2} \cdot \text{Pr}^{1/3}}{\left(1 + \left(\frac{0.4}{\text{Pr}}\right)^{2/3}\right)^{1/4}}\left(1 + \left(\left(\frac{\text{Re}_D}{282000}\right)^{5/8}\right)^{4/5}\right)\right) \tag{5.6}$$

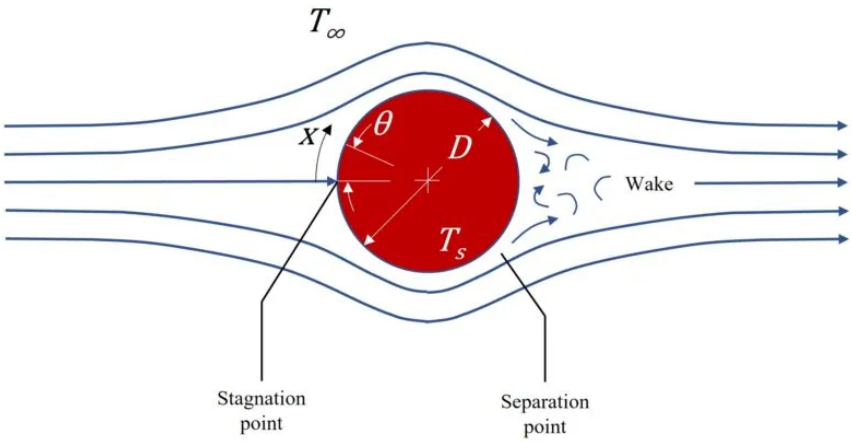

Figure 5.7: Fluid flow around a cylinder, lateral view [51]

Reynolds and Prandtl are dimensionless parameters which characterize the flow and the thermal behaviour of the fluid. Another loss parameter to account for was the **radiative losses**, which will be calculated analytically from equation 2.11. The emissivity was found to be 0.83 for the black SiC at low temperatures [52]. The average temperature data were gathered and the values were used in the

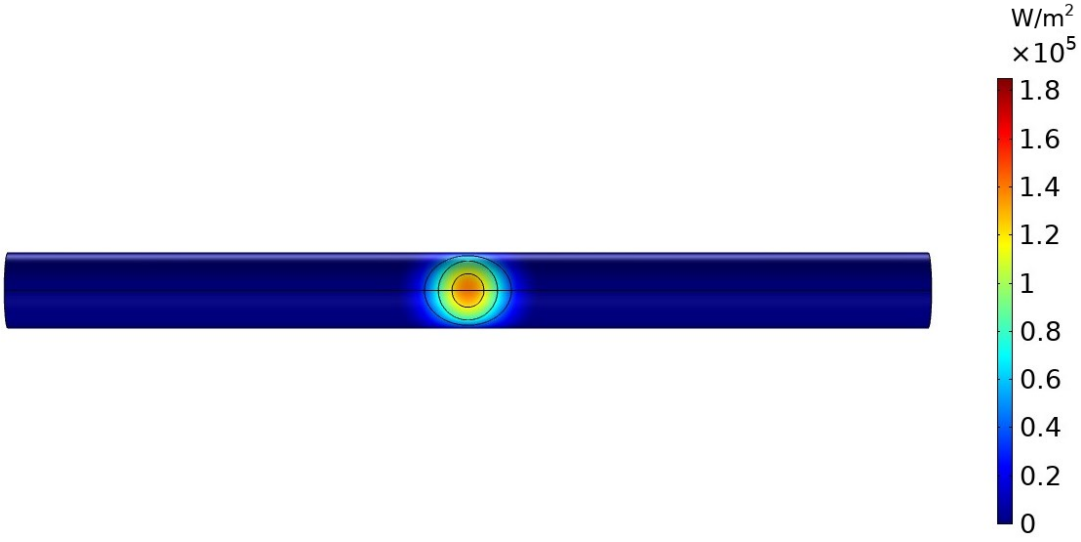

Figure 5.8: Thermal dispersion model with losses by wind convection and radiation

equation for each area of the domain. The radiative flux was then set as outgoing power in the corresponding areas. In the end the receiver model accounting for losses is shown in Figure 5.8. As expected, the deposited power in the real case is

lower with respect to the optical model of Figure 5.5 due to the additional sources of loss. After preparing the receiver model, it needs to be tested in a transient study chosen from 8:00 to 16:00, as significant solar radiation during late autumn falls within that range (in COMSOL it will be a 28800 s transient simulation). The choice of the temperature measurement point to be compared with real-case measurements also needs to be made. The thermocouple measurement is analogous to the hollow cylinder of the receiver model as it provides a point measurement. However, the thermocouple was not placed at the focal point to avoid disturbing the reflection dynamics of the rays, so the measured data is not related to the maximum temperature in the receiver but to a lower one. Therefore, an arbitrary point to the left of the focal point was chosen, which still had satisfactory radiation but did not reach the higher temperatures of the central point (Figure 5.9). The transient

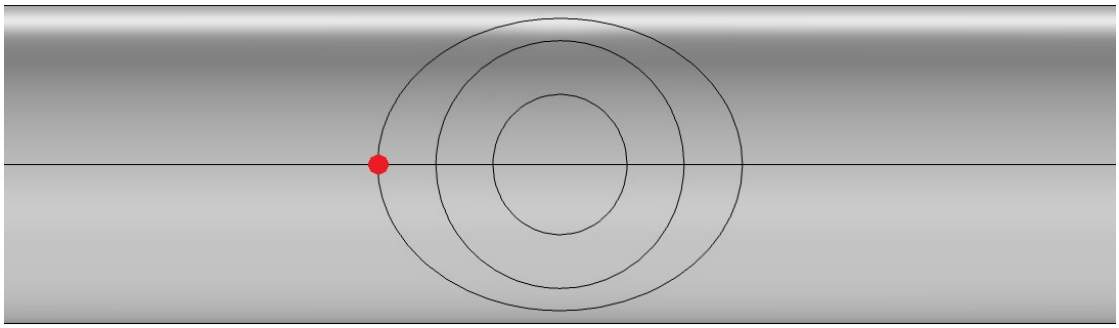

Figure 5.9: Point selection for experimental data comparison

study was then set up, choosing the average temperatures measured for the ATL SiC receiver as the reference temperatures. Since temperature data is available for late October, some days in November, and a few days in early December, the case study could be considered as a modeling of the receiver based on November temperatures. The study is presented in Figure 5.10. Regarding the discrepancy between the model and experimental data, the *Mean Absolute Percentage Error (MAPE)* was used, which indicates the average percentage difference between the target values (the experimental data) and the values obtained from the model. The absolute value of the relative error of each point is calculated first, and then the average of all values is evaluated according to the following formula:

$$MAPE = \frac{1}{n}\sum_{t=1}^{n}\left|\frac{A_t - F_t}{A_t}\right| \tag{5.7}$$

being the A_t actual value of the model and F_t the forecast value of the experimental data. The very first points of the curve were neglected as the uncertainty of

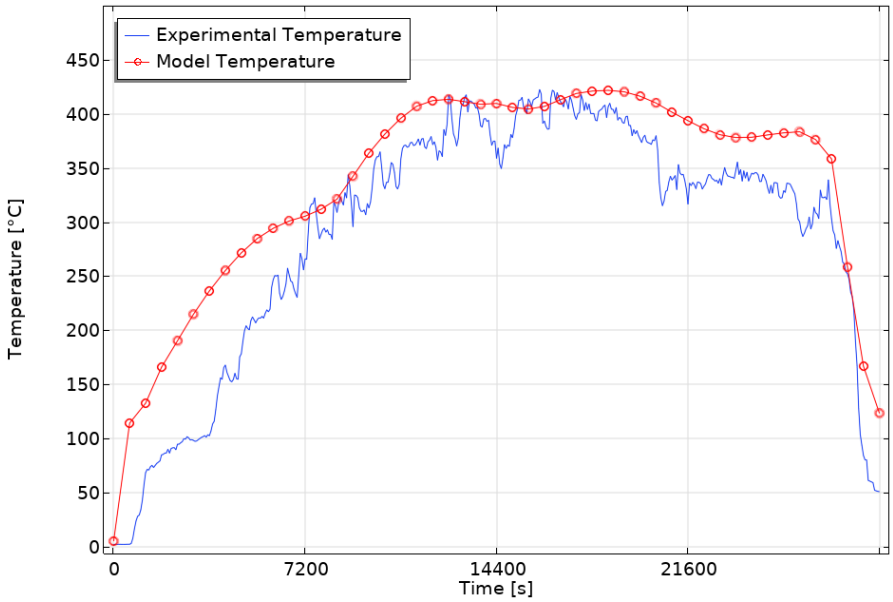

Figure 5.10: Temperature obtained by the model compared to the experimental one

thermocouple N is much greater there. In this curve, the MAPE is approximately 18%, with peaks of relative errors mainly in the initial part of the curve, reaching a maximum of 56% at 3600 s from the start of the simulation. Considering this is a preliminary analysis of a potential prototype, with measurements available only at one point and considering the complexity of the analyzed problem, the error seems acceptable. Another factor to consider is the similarity of the model to real behavior. In this case, the model manages to closely follow the various phases of the receiver, with an initial phase of temperature increase from ambient temperature, a central phase at high temperature (which is used for storage charging and actual production), and a final phase of temperature decrease. Given the accuracy of the model created, which manages to reproduce the real conditions quite well, it is therefore possible to proceed with the integration of the phase change material and the heat transfer fluid.

5.3 PCM arrangement

Regarding the accommodation of the PCM, several configurations have been considered. The first one hypothesized involved encapsulating the PCM material in spheres (Figure 5.11). Therefore, 7 spheres with a diameter of approximately 5 mm were arranged along the receiver section throughout its length to occupy the entire receiver. The heat transfer fluid is supposed to pass through the spaces

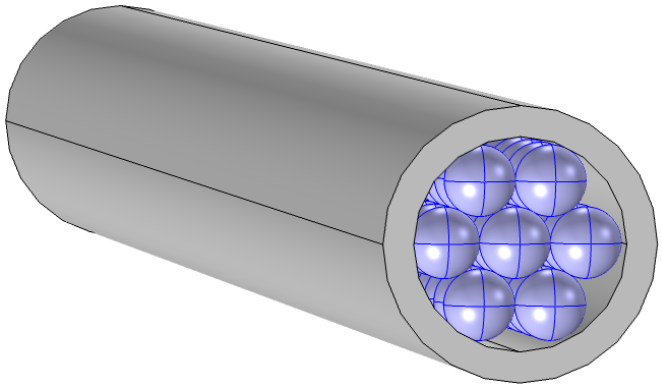

Figure 5.11: Configuration with spherical encapsulated PCM in blue

left between the spheres and the receiver wall. Another configuration that has been considered is one with a phase change material having the same shape as the receiver, that is a hollow cylinder with an outer diameter that matches the inner diameter of the receiver (Figure 5.12). The PCM can be encapsulated in a tube that still allows the passage of the heat transfer fluid through the center for heat removal. The configuration of the first case is based on a more established

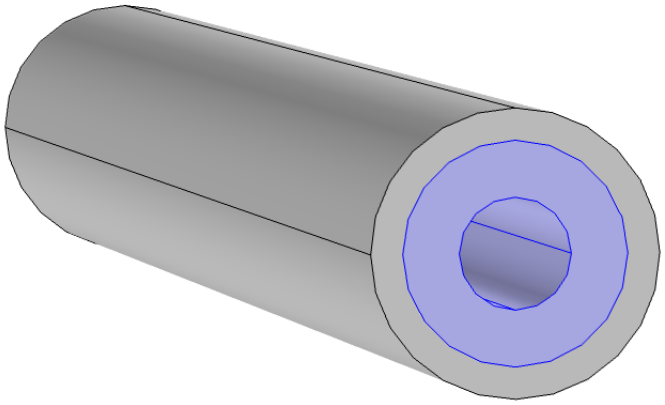

Figure 5.12: Configuration with tubular encapsulated PCM in blue

encapsulation technology, as spheres are one of the most commonly used forms for encapsulation. To contain them internally, grids could be used at the inlet and outlet of the receiver to allow containment and passage of the fluid. The reason why it was avoided as a final configuration lies mainly in the turbulence that the configuration would induce in the heat transfer fluid due to the arrangement of the spheres, which in turn would cause vibrational stress to the receiver, reducing its lifespan. The second configuration was also discarded mainly due to the issue

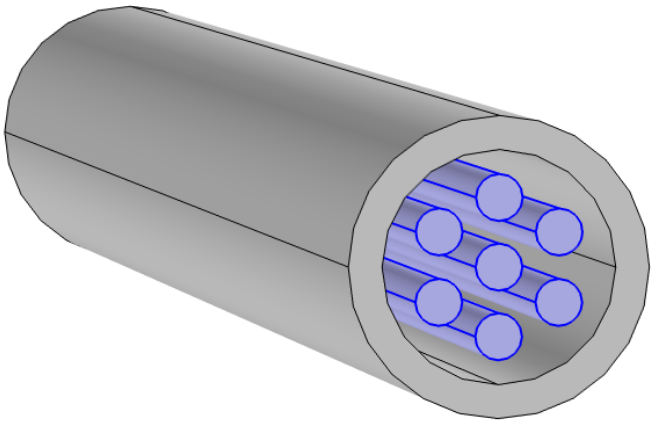

Figure 5.13: Configuration with cylindrical encapsulated PCM in blue

of thermal expansion of the encapsulated PCM, which would create mechanical stress on the external receiver, as well as the difficulty of encapsulating it in an hollow cylinder. The final configuration chosen is shown in Figure 5.13. The open space surrounding the cylindrical PCM helps to reduce pressure drop within the receiver. By allowing for smoother fluid flow with minimized resistance, this configuration reduces the energy required for fluid circulation, contributing to operational cost reduction and a more homogeneous heat removal. In addition to the reduced pressure drop, the circulating fluid also prevent high turbulence vibrational stress on the receiver. This design also offers benefits in terms of mechanical stability and ease of manufacturing and maintenance. Unlike a stack of closely packed spheres, which may create localized stress points, the cylindrical configuration distributes mechanical stresses more evenly along the length of the receiver, enhancing structural integrity and longevity. Furthermore, the simpler fabrication and maintenance procedures associated with cylindrical PCM designs make easier the system installation and removal for possible interventions. Also the material dilatation does not affect the receiver walls anymore in the perspective of further stresses. Each PCM cylinder has a diameter of 3 mm. For the cylinders support, it could be used a spacing device for the seven tubes at the inlet and the outlet or some thin support brackets to minimize fluid flow obstruction.

5.4 PCM Model

For the current choice of PCM, the previous study is actually insufficient, as analyses were only conducted at the surface of the receiver near the focal point. Naturally, at the borders and inside the receiver, the temperature will tend to be much lower due to the distance from the irradiation spot, and the conductive and

convective thermal movements within the body. Furthermore, it is necessary to consider that ideally, obtaining a phase change in the PCM as extensive as possible would be optimal for its best utilization, even at the expense of selecting lower temperatures for the phase change temperature. For a preliminary analysis is has been chosen $LiNO_3$, lithium nitrate, a salt used as a phase change material due to its high latent heat and its ability to undergo phase transitions at a specific temperature. The high temperature would allow to exploit a heat resource with

Material	**Melting temperature (°C)**	**Melting enthalpy (kJ/kg)**	**Thermal conductivity (W/mK)**	**Density (kg/m^3)**
$LiNO_3$	254	360	0.58 (liquid) 1.37 (solid)	1780 (liquid) 2140 (solid)

Table 5.1: Properties of $LiNO_3$ [30]

higher energy, and the thermal conductivity of the material is elevated, especially in the solid state. Regarding encapsulation, since $LiNO_3$ is an organic material, it could have compatibility issues with other materials, exhibiting chemical reactivity and corrosion. Expanded vermiculite (EVM), a mineral that undergoes expansion at elevated temperatures, resulting in high porosity and a significant specific surface area, has been considered due to its complete compatibility with $LiNO_3$, as well as with $NaNO_3$ and KNO_3 [53]. Chosen the PCM, it was subsequently implemented in COMSOL. To implement it and consider the phase change from solid to liquid, it is necessary to use the heat transfer module in solids and fluids. The PCM must be initialized with both solid and liquid values, indicating in the phase change module the phase transition temperature, latent heat, and properties of the two phases. For the process of phase change the following equation is applied at the interface [54]:

$$k_{\text{sol}}\nabla T_{\text{sol}} - k_{\text{liq}}\nabla T_{\text{liq}} = \rho\Delta h_{\text{fus}}\frac{dx}{dt} \tag{5.8}$$

where x is the melting interface position and ∇ denotes the gradient on the interface. Regarding the heat transfer fluid, it was considered to use air due to its ease of use and availability, although its thermal conductivity is not as high. Liquids such as water were discarded because they would require more energy for pumping and would have the issue of managing the phase change to steam once heated. The model is shown in Figure 5.14, having been centrally longitudinally sectioned to reduce computational cost. In the schematic, the SiC material of the receiver is indicated in black, the heat transfer fluid in blue, and the phase change material bars in red. As a first approximation for a simpler model, air is assumed to be a still fluid, meaning that during the charging phase sensible energy recovery in the

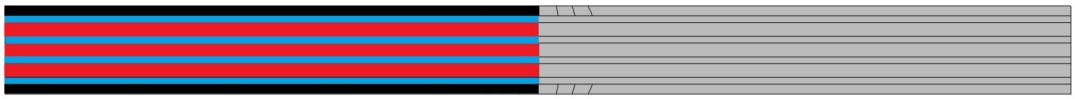

Figure 5.14: Central longitudinal section of the model, with black being the receiver material, blue the heat transfer fluid and red the PCM

receiver is not allowed. The energy could only be retrieved during the discharging phase in that configuration. Additionally, the outer shell of the PCM encapsulation is not considered, again for model simplification, as it is assumed to be extremely thin with good thermal conductivity. The Figure 5.15 figure shows different time

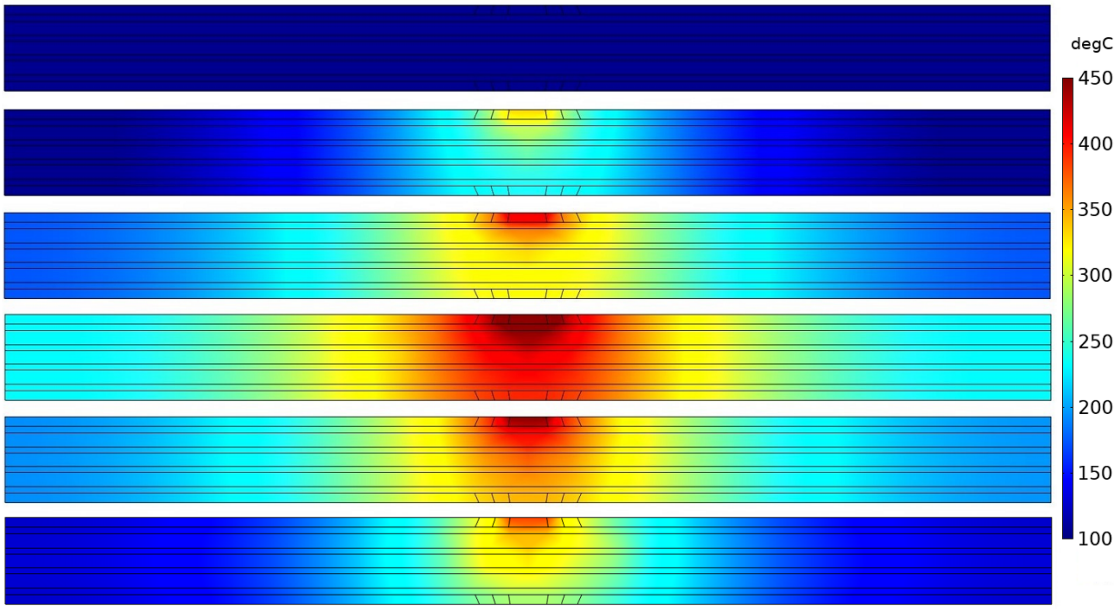

Figure 5.15: Central longitudinal section of the model at different time steps

steps of the model, from the initial conditions at 5°C, passing through the maximum temperature up to the final configuration. Each time step was performed every 10 minutes, and those represented in the figure are at times 0, after 90, 170, 320, 390, and 450 minutes. As can be seen, since the configuration is symmetric along the axis, the thermal evolution is identical on the left and right sides of the central point. The contribution of PCM to heat storage is not clearly visible because latent heat depends on the amount of material undergoing phase change, and in our case, the amount of PCM is minimal, so phase change occurs quickly and in a localized manner. Another limiting factor is the 10 minute time step, which does not allow

for a more detailed view of changes that occur over shorter periods, as in the case of $LiNO_3$ in the study. The last of the figures represents the moment when we stop for the assessment of PCM utilization in the system, that is 7 hours and a half after the start of the simulation, at 15:30, because from this point onwards, solar radiation decreases significantly, but the effect of wind convection and radiative losses continues to extract heat from the receiver and discharging the PCM. The

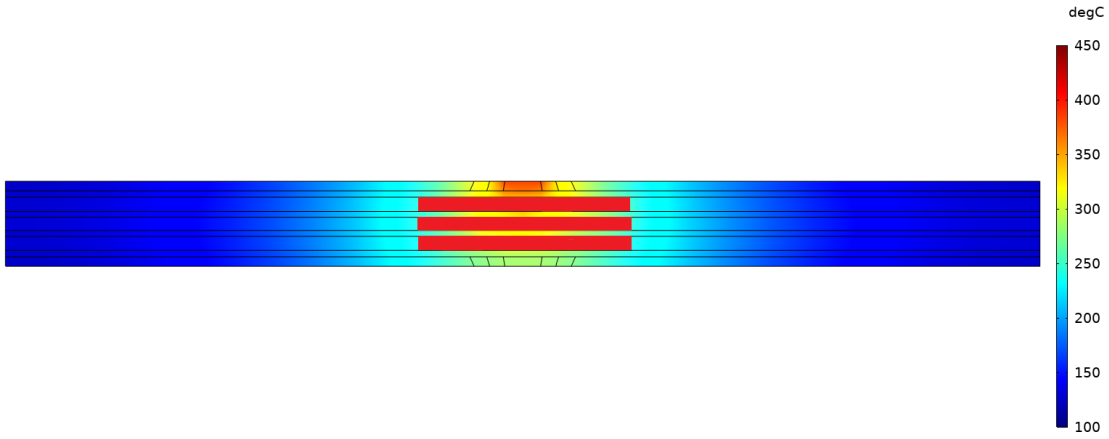

Figure 5.16: In red, charged PCM at the end of the time dependent study

final result regarding the use of $LiNO_3$ is shown in Figure 5.16. To evaluate the quantity of material that has melted, it was used the COMSOL *Phase Indicator 2-1* function on the volume of the PCM, which indicates the percentage of material where phase change has occurred. Only $\sim 20\%$ of the material has been successfully charged and allows for subsequent discharge. In this case, the model cannot be considered effective as it does not allow the use of heat during the charging phase, causing a large amount of heat loss that could be partly avoided with a circulating heat transfer fluid in the system. Furthermore, fluid movement could lead to a more uniform temperature distribution throughout the receiver and a reduction of thermal stresses.

5.5 PCM Model with Heat Transfer Fluid flow

In order to account for fluid movement, the *Laminar Flow* physics is included in the model. After initializing the fluid, a circulation velocity of 0.4 m/s and an exit pressure loss equal to zero was chosen. The direction of the motion is indicated in Figure 5.17, with the air in blu and the arrows indicating the entering cold fluid and the exiting of hot one. The fluid was set with an inlet condition of 15°C and for the interaction with the walls, a no-slip condition was selected. The equations that

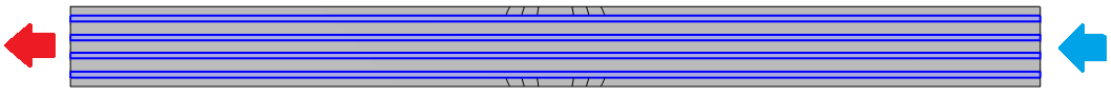

Figure 5.17: Direction of the fluid motion with the air in blue

need to be solved to characterize the laminar flow are the *Continuity Equation* and the *Navier-Stokes Equation*, expressing the mass conservation and the description of a viscous fluid motion. The fluid, as an approximation, is considered to have a small variation in density during operation, in order to simplify the equations as follows:

$$\nabla \cdot u = 0 \tag{5.9}$$

$$\rho \frac{\partial u}{\partial t} + \rho u(u \cdot \nabla) = -\nabla p + \mu \nabla^2 u \tag{5.10}$$

Regarding the PCM material, another selection needs to be made. The previous phase change material was only utilized to 20%, and by introducing an air flow into the model, temperatures will further decrease due to convective heat exchange with the fluid. Therefore, a material with a much lower melting point than the current one should be chosen. Thus, a eutectic mixture of 67% KNO_3 and 33%

Material	**Melting temp. (°C)**	**Melting enthalpy (kJ/kg)**	**Thermal conductivity (W/(mK))**	**Density (kg/m^3)**
67% KNO_3 + 33% $LiNO_3$	133	170	0.85-0.95 (liquid) 1.35-1.45 (solid)	1850(liquid) 2350 (solid)

Table 5.2: Properties of 67% KNO_3 + 33% $LiNO_3$

$LiNO_3$, with a melting temperature of 133°C, was opted for, resulting in reduced latent heat (170 kJ/kg) owing to the considerably lower temperature compared to the prior scenario [30]. The values are reported in Table 5.2. The behavior of the new PCM chosen can be visualized in Figure 5.18. The figure represents the temperature trend by vertically cutting through the cylinder of the central phase change material. The initial evolution on the x-axis is the heat transfer fluid closest to the focal area, followed by the section of the actual PCM, and finally the lower fluid. The various lines represented are the visualization time steps of the model every 20 seconds. Once the material reaches the phase change point at 133°C, the temperature increase is no longer gradual, but in the center there is a constant temperature for various time steps, moving gradually to the right, while in the meantime, the temperature of the heat transfer fluid increases slightly

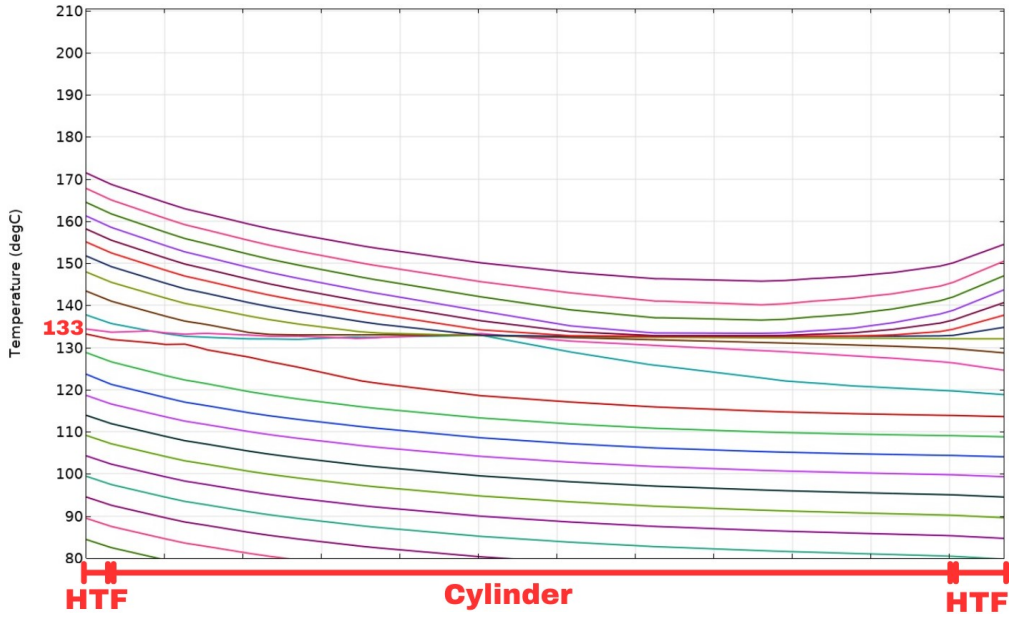

Figure 5.18: Graphic of the PCM cylinder behaviour during melting

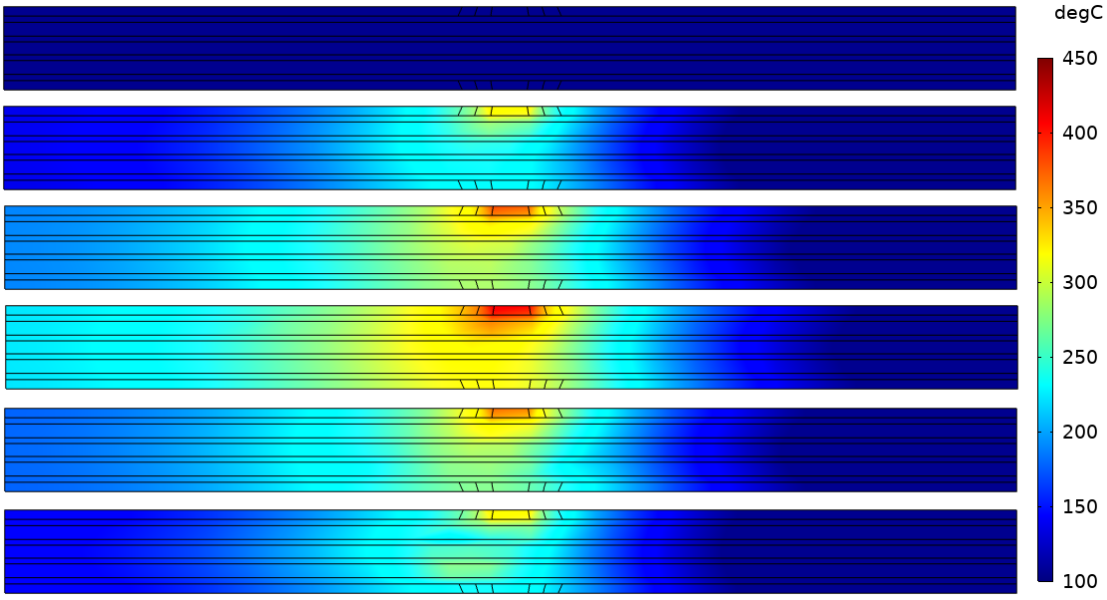

Figure 5.19: Central longitudinal section of the model at different time steps with heat transfer fluid flow

both on the right and left of the graphic. The time frame for phase change is not high as the amount of phase change material is minimal, and therefore, so is

the associated latent energy. After fully characterizing the model, it was run for 8 hours, 28800 s, as before. The results are shown in Figure 5.19. The thermal arrangement is no longer symmetrical as in the previous case, since the air tends to shift the thermal interface to the left. Another significant effect is the cooling of the right side of the receiver due to the entry of cold fluid, which gradually warms up as it progresses inside the receiver. As predicted, the temperatures reached are

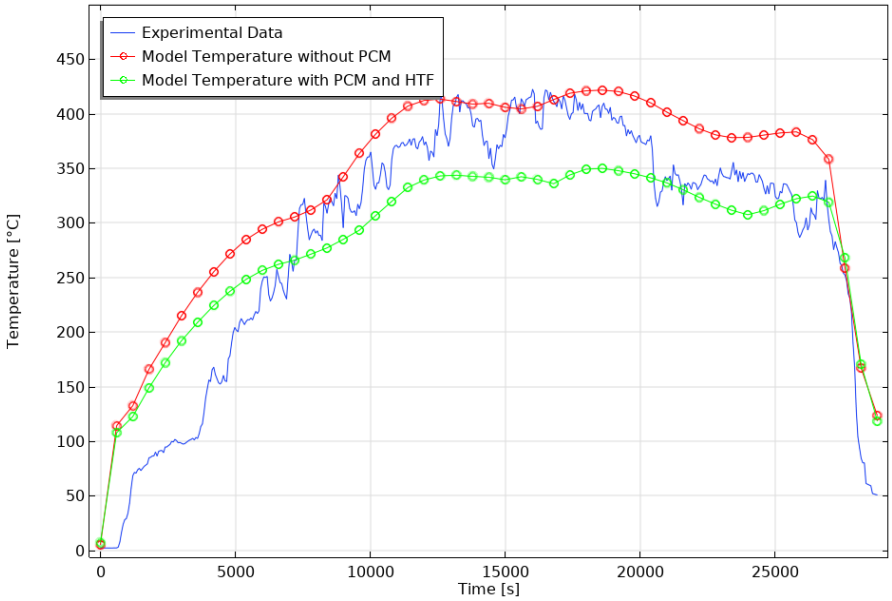

Figure 5.20: Temperature obtained by the model compared to the experimental one

much lower with respect to the previous case, however, it is possible to exploit the sensible heat extracted at every moment from the heat transfer fluid. To calculate it, the Formula 3.2 with mass flow can be used between the averaged temperature at inlet and outlet. Taking into account the point near the focal area considered previously, the temperature curve obtained has a temperature trend similar to the previous one of the receiver without PCM and HTF, but with significantly reduced values due to the heat absorbed by the air and the phase change material (Figure 5.20). Regarding the percentage of phase change material utilized in this case, despite the temperature having decreased significantly, by choosing a material with a much lower melting temperature, the final utilization is much more efficient. In fact, there is a 65% of material loaded at the end of the transient period (Figure 5.21). The Table 5.3 therefore reports all the values of the instant power from sensible heat extracted by the heat transfer fluid during solar irradiation.

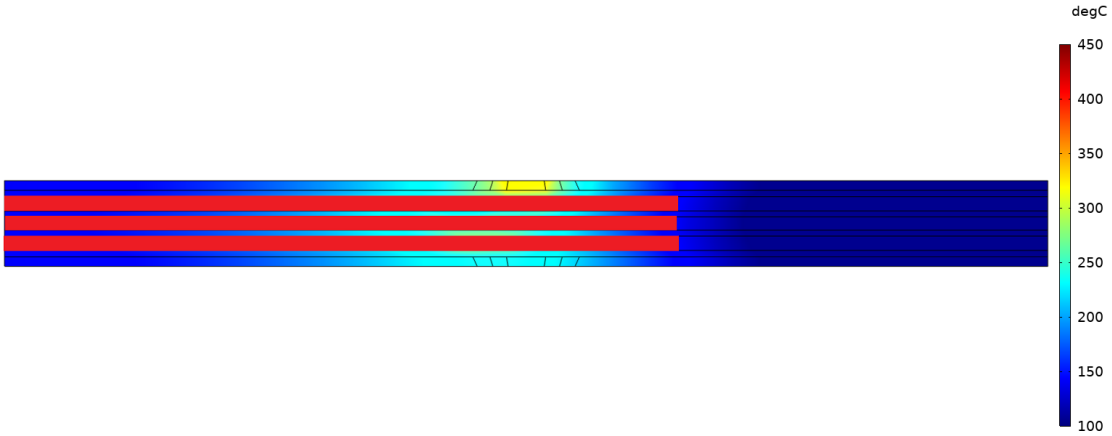

Figure 5.21: In red, charged PCM at the end of the time dependent study with heat transfer fluid flow

Time Steps (s)	**Inlet Temp. (°C)**	**Outlet Temp. (°C)**	$\dot{\mathbf{Q}}$**sens (W)**
600	11.2	23.8	0.66
1200	11.2	27.4	0.83
1800	11.9	37.2	1.30
2400	13.2	50.1	1.91
3000	14.6	63.6	2.53
3600	16.1	76.8	3.13
4200	17.7	89.8	3.72
4800	19.3	101.5	4.25
5400	20.6	111.7	4.70
6000	21.8	119.8	5.06
6600	22.6	125.6	5.32
7200	23.2	129.7	5.50
7800	23.9	134.7	5.72
8400	24.8	140.4	5.97
9000	26.4	150.8	6.43
9600	28.1	161.3	6.88
10200	30.0	173.0	7.39
10800	31.8	184.8	7.90
11400	33.6	196.4	8.41
12000	34.9	204.9	8.78
12600	35.6	209.9	9.01
13200	35.7	211.4	9.08
13800	35.5	211.3	9.08

Time Steps (s)	**Inlet Temp. (°C)**	**Outlet Temp. (°C)**	$\dot{Q}$**sens (W)**
14400	35.5	209.7	9.00
15000	35.2	206.0	8.82
15600	35.3	203.0	8.66
16200	35.6	203.9	8.69
16800	34.9	204.4	8.76
17400	35.8	209.3	8.96
18000	36.9	212.1	9.06
18600	37.1	215.2	9.20
19200	36.9	214.5	9.17
19800	36.5	211.0	9.02
20400	35.7	207.3	8.86
21000	34.8	202.8	8.68
21600	33.9	196.6	8.41
22200	32.9	189.6	8.10
22800	32.1	183.4	7.82
23400	31.3	177.7	7.56
24000	30.8	174.6	7.43
24600	30.9	177.0	7.55
25200	31.4	181.6	7.76
25800	31.9	186.0	7.96
26400	32.0	187.9	8.05
27000	30.9	181.6	7.79
27600	23.0	135.8	5.83
28200	14.5	61.6	2.43
28800	11.3	27.8	0.85

Table 5.3: Power from sensible heat retrieved by the heat transfer fluid

The instantaneous power available from the heat transfer fluid in each time step is very low due to the low mass flow rate, considering the small spaces occupied in the receiver by air. In Table 5.4 instead, the energy extractable from the PCM at the end of the charge is reported, evaluated with the Formula 3.3 for the liquid part till the melting point, the latent heat and the solid part till a minimum temperature considered for power extraction, 50°C. For the liquid part an averaged final temperature was evaluated. To fully discharge the cylinder, it is possible to first utilize the sensible part associated with the liquid, then the latent part by bringing the PCM back to solid phase, and finally the latent heat associated with the solid part. Assuming the cylinder is discharged after the end of the solar

Qsens(liq) (kJ)	Qlat (kJ)	Qsens(sol) (kJ)	Qtot (kJ)
1.14	2.23	1.35	4.71

Table 5.4: Energy stored in the Phase Change Material

radiation, and accounting for the highest instantaneous power during operation, which is 0.92 W, the discharge process would take approximately 9 minutes. This time frame is indicative of the decoupling process between radiation and energy availability. Although the decoupling time may seem negligible, it is important to consider that the constructed model represents a prototype stage and is on a small scale, representing only a potential real thermal storage application. Furthermore, it can certainly be improved with the right adjustments, from selecting a more efficient phase change material to arranging the entire receiver-storage system more efficiently. Another heat transfer fluid can also be used for heat exchange, such as a gas with higher thermal conductivity or a liquid if the pumping system can be managed better and avoid phase change inside the loop.

5.6 Organic Rankine Cycle integration

One of the best ways to exploit a low-temperature heat source with variable thermal inputs is the *Organic Rankine Cycle (ORC)*. This cycle utilizes an organic fluid, which has a high molecular weight and low boiling point to allow for vaporization also at low temperatures and small volumes at the turbine. Cycles that use water

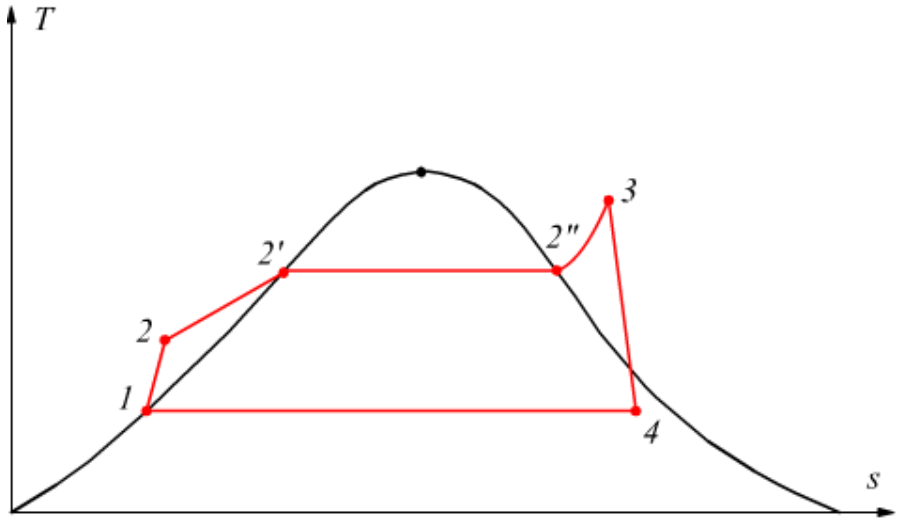

Figure 5.22: Real Rankine Cycle schematic [55]

as the circulating fluid instead require higher temperatures for vaporization and suffer from low efficiency at lower temperature ranges. The basic operation of the ORC involves converting thermal energy into mechanical energy and eventually producing electricity. The various cycle steps are schematized in Figure 5.22 and can be summarized in [55]:

1–2 : Adiabatic compression of the liquid, not a reversible transformation since the increase in entropy is accounted for by the pump efficiency η_p

2–2' : Heating at constant pressure of the fluid until the saturation temperature

2'–3 : Vaporization at constant pressure until the state of superheated saturated vapor

3–4 : Irreversible adiabatic expansion, with a loss evaluated by the turbine efficiency η_t

4–1 : Heat removal at constant pressure until returning to the initial condition of saturated liquid

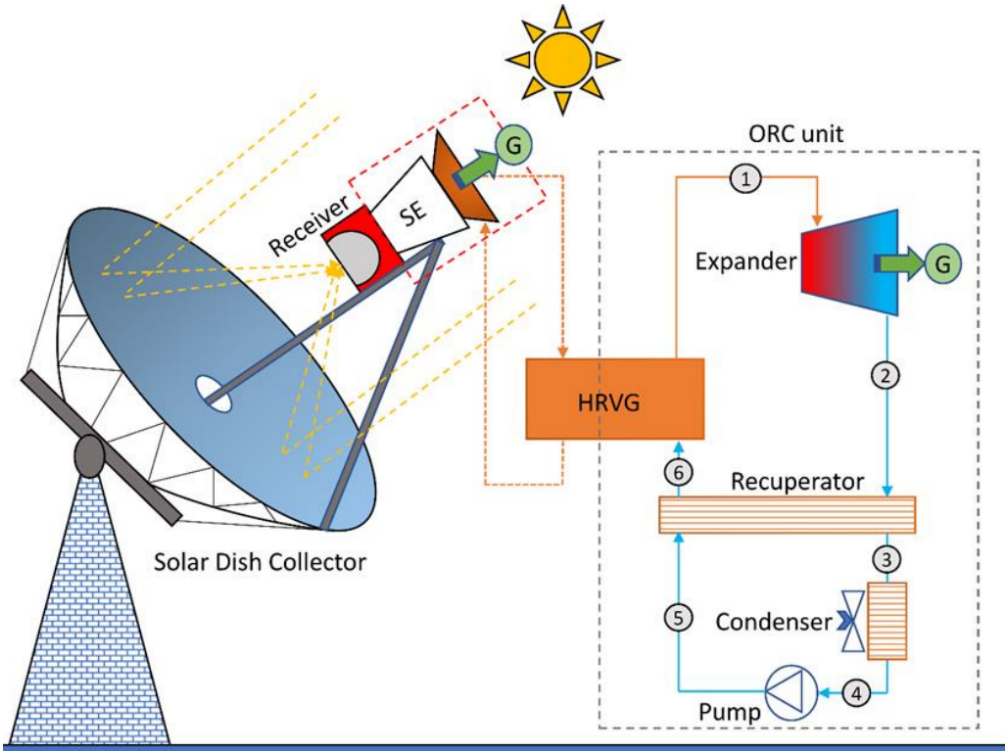

Figure 5.23: Diagram of a solar dish coupled to an ORC-Stirling Engine system [56]

Instead, a diagram of the cycle with its various components is displayed in Figure 5.23. Regarding the Rankine cycle, the heat transfer fluid reaches the Heat Recovery Vapor Generator (HRVG), designed to evaporate the working fluid of the ORC (Organic Rankine Cycle). This corresponds to the 2-3 phase in the schematic. The steam then goes into the turbine for expansion, reducing its pressure and temperature. In this cycle, a recuperator has been inserted, which serves to preheat the liquid between the pump outlet and the turbine outlet. The liquid is then totally condensed by an air or liquid heat sink and finally reaches the pump where it increases its pressure. It is preheated by the recuperator and the cycle restarts, retrieving heat from the solar HTF in the heat exchanger. The turbine is coupled to an electric generator through a shaft. The rotational motion of the shaft due to the vapour expansion induces an electromagnetic field within the generator, leading to the generation of electricity.

Chapter 6

Conclusions

This master's thesis dealt with the comprehensive modeling of a solar receiver within a solar dish system, coupled with phase change material for thermal storage. Experimental temperature measurements were conducted on various materials, including alumina, BJS SiC, and ATL SiC. While the alumina exhibited structural fragility and the BJS SiC showed insufficient temperatures, the ATL SiC material emerged as the most promising receiver material, reaching temperatures suitable for energy conversion applications.

The modeling efforts, conducted using COMSOL Multiphysics, included the development of a ray optics model to analyze power distribution on the receiver and a thermal dispersion model to account for all sources of heat loss. A transient study from 8:00 to 16:00 was conducted to compare the model to average experimental data. The model exhibited a Mean Absolute Percentage Error (MAPE) of approximately 18%, considered acceptable given the inherent complexities of the system, the limited experimental data availability and assumptions regarding environmental factors.

Subsequent iterations of the model incorporated PCM integration to allow for thermal storage. Initial attempts with still air as heat transfer fluid and $LiNO_3$ PCM proved suboptimal due to operational constraints, leading to the adoption of a 67% KNO_3 + 33% $LiNO_3$ PCM mixture with a lower melting temperature and latent heat. The addition of laminar airflow further optimized the system thermal exploitation, and, although the internal temperatures have decreased, in general PCM was better employed.

Despite challenges such as low power generation from sensible heat due to the unsuitable time of year for testing with solar radiation, limited mass flow and the relatively small size of the cylinder, the corresponding calculated discharge time of the PCM could be promising, indicating its potential for effective energy decoupling. While the results have limitations, such as the prototype's scaled-down nature and inherent modeling inaccuracies, the thesis underscores the viability of

thermal PCM storage as a means of enhancing solar energy utilization. Moreover, it points out the importance of further research and optimization, paving the way for more efficient and sustainable solar energy systems in the future.

Bibliography

[1] Brian R Keeble BSc Mbbs Mrcgp. «The Brundtland report: 'Our common future'». In: *Medicine, Conflict and Survival* 4 (1987), pp. 17–25. URL: https://api.semanticscholar.org/CorpusID:108488622 (cit. on p. 1).

[2] Copernicus Press release. «Summer 2023: the hottest on record». In: *Copernicus Climate Change Service* (2023). URL: https://climate.copernicus.eu/summer-2023-hottest-record (cit. on pp. 1, 2).

[3] Krista Myers, Peter Doran, John Cook, John Kotcher, and Teresa Myers. «Consensus revisited: quantifying scientific agreement on climate change and climate expertise among Earth scientists 10 years later». In: *Environmental Research Letters* 16 (2021). DOI: 10.1088/1748-9326/ac2774 (cit. on pp. 2, 3).

[4] Parties of the 1992 UNFCCC Convention. *United Nations framework convention on climate change*. 1992. URL: https://unfccc.int/files/essential_background/background_publications_htmlpdf/application/pdf/conveng.pdf (cit. on p. 2).

[5] Brad Plumer and Vivian Nereim Lisa Friedman. «Saudi Arabia Is Trying to Block a Global Deal to End Fossil Fuels, Negotiators Say». In: *The New York Times* (2023). URL: https://www.nytimes.com/2023/12/10/climate/saudi-arabia-cop28-fossil-fuels.html (cit. on p. 3).

[6] Lisa Friedman. «Climate Summit Leader Tries to Calm Uproar Over a Remark on Fossil Fuels». In: *The New York Times* (2023). URL: https://www.nytimes.com/2023/12/04/climate/cop28-aljaber-fossil-fuels.html (cit. on p. 3).

[7] Adam Morton. «Cop28: Australia, US and UK say they won't sign agreement that would be 'death certificate' for small islands». In: *The Guardian* (2023). URL: https://www.theguardian.com/environment/2023/dec/12/cop-28-australia-us-and-uk-say-they-wont-sign-agreement-that-would-be-death-certificate-for-small-islands (cit. on p. 3).

[8] The Conference of the Parties serving as the meeting of the Parties to the Paris Agreement. *Outcome of the first global stocktake*. 2023. URL: https://unfccc.int/documents/636608 (cit. on p. 3).

[9] UN Climate Press. «COP28 Agreement Signals "Beginning of the End" of the Fossil Fuel Era». In: *United Nations Framework Convention on Climate Change* (2023). URL: https://unfccc.int/news/cop28-agreement-signals-beginning-of-the-end-of-the-fossil-fuel-era (cit. on p. 4).

[10] UN Climate Press. «The Paris Agreement». In: *United Nations Framework Convention on Climate Change* (2020). URL: https://unfccc.int/process-and-meetings/the-paris-agreement (cit. on p. 4).

[11] Nuclear Energy Agency. «COP28 recognises the critical role of nuclear energy for reducing the effects of climate change». In: *Nuclear Energy Agency* (2023). URL: https://www.oecd-nea.org/jcms/pl_89153/cop28-recognises-the-critical-role-of-nuclear-energy-for-reducing-the-effects-of-climate-change (cit. on p. 5).

[12] UN nations. *THE 17 GOALS*. URL: https://sdgs.un.org/goals (cit. on p. 5).

[13] IEA. «World Energy Outlook 2023». In: *IEA, Paris* (2023). License: CC BY 4.0 (report); CC BY NC SA 4.0 (Annex A). URL: https://www.iea.org/reports/world-energy-outlook-2023 (cit. on pp. 5, 6).

[14] Carols Guillermo Ruiz Sánchez. *Evaluation of the Operational Performance of a Parabolic Trough CSP Plant*. 2013. URL: https://www.diva-portal.org/smash/get/diva2:681144/FULLTEXT01.pdf (cit. on p. 7).

[15] IEA. «Energy Statistics Data Browser». In: *IEA, Paris* (2023). URL: https://www.iea.org/data-and-statistics/data-tools/energy-statistics-data-browser (cit. on p. 8).

[16] IEA. «Technology Roadmap - Concentrating Solar Power». In: *IEA, Paris* (2010). License: CC BY 4.0. URL: https://www.iea.org/reports/technology-roadmap-concentrating-solar-power (cit. on p. 9).

[17] Abdul Ghani Olabi. *Renewable Energy - Volume 1 : Solar, Wind, and Hydropower*. Academic Press, 2023. DOI: https://doi.org/10.1016/C2021-0-02341-5 (cit. on p. 10).

[18] O Achkari and A El Fadar. «Latest developments on TES and CSP technologies – Energy and environmental issues, applications and research trends». In: *Applied Thermal Engineering* 167 (2020), p. 114806. ISSN: 1359-4311. DOI: https://doi.org/10.1016/j.applthermaleng.2019.114806. URL: https://www.sciencedirect.com/science/article/pii/S1359431118363269 (cit. on p. 10).

[19] Gabriel Morin, Jürgen Dersch, Werner Platzer, Markus Eck, and Andreas Häberle. «Comparison of Linear Fresnel and Parabolic Trough Collector power plants». In: *Solar Energy* 86 (1 2012), pp. 1–12. ISSN: 0038-092X. DOI: https://doi.org/10.1016/j.solener.2011.06.020. URL: https://www.sciencedirect.com/science/article/pii/S0038092X11002325 (cit. on p. 10).

[20] R. P. Merchán, M. J. Santos, A. Medina, and A. Calvo Hernández. *High temperature central tower plants for concentrated solar power: 2021 overview*. Mar. 2022. DOI: 10.1016/j.rser.2021.111828 (cit. on p. 11).

[21] Susant Kumar Sahu, Arjun Singh Kopalakrishnaswami, and Sendhil Kumar Natarajan. «Historical overview of power generation in solar parabolic dish collector system». In: *Environmental Science and Pollution Research* 29 (43 2022), pp. 64404–64446. ISSN: 1614-7499. DOI: 10.1007/s11356-022-21984-3. URL: https://doi.org/10.1007/s11356-022-21984-3 (cit. on p. 11).

[22] Matthias Günther, Reza Shahbazfar, Thomas Fend, and Mohammad Hamdan. «Advanced CSP Teaching Materials Chapter 7 Solar Dish Technology». In: 2011. URL: https://api.semanticscholar.org/CorpusID:140125674 (cit. on pp. 12–17, 19).

[23] Keith Lovegrove and Wes Stein. *Concentrating Solar Power Technology: Principles, Developments, and Applications*. Elsevier, Jan. 2020, pp. 1–778. ISBN: 9780128199701. DOI: 10.1016/B978-0-12-819970-1.09991-6 (cit. on pp. 13, 18, 21).

[24] Manuel Romero, Reiner Buck, and James E. Pacheco. «An Update on solar central receiver systems, projects, and technologies». In: *Journal of Solar Energy Engineering, Transactions of the ASME* 124 (2 May 2002), pp. 98–108. ISSN: 01996231. DOI: 10.1115/1.1467921 (cit. on p. 17).

[25] Clifford K. Ho and Brian D. Iverson. «Review of high-temperature central receiver designs for concentrating solar power». In: *Renewable and Sustainable Energy Reviews* 29 (Jan. 2014), pp. 835–846. ISSN: 1364-0321. DOI: 10.1016/J.RSER.2013.08.099 (cit. on p. 18).

[26] Roberta Mancini. *Volumetric Solar Receiver for a Parabolic Dish and Micro-Gas Turbine system Design, modelling and validation using Multi-Objective Optimization*. 2015 (cit. on p. 18).

[27] Philipp Good, Thomas Cooper, Marco Querci, Nicolay Wiik, Gianluca Ambrosetti, and Aldo Steinfeld. «Spectral reflectance, transmittance, and angular scattering of materials for solar concentrators». In: *Solar Energy Materials and Solar Cells* 144 (Jan. 2016), pp. 509–522. ISSN: 0927-0248. DOI: 10.1016/J.SOLMAT.2015.09.057 (cit. on p. 19).

[28] Petr, Unger Hermann Mohr Markus, and Svoboda. «Solarturmkraftwerke». In: Springer Berlin Heidelberg, 1999, pp. 121–172. ISBN: 978-3-642-58489-3. DOI: 10.1007/978-3-642-58489-3_4. URL: https://doi.org/10.1007/978-3-642-58489-3_4 (cit. on pp. 20, 21).

[29] Ibrahim Dincer and Marc Rosen. *Thermal Energy Storage: Systems and Applications*. Feb. 2021. ISBN: 9781119713159. DOI: 10.1002/9781119713173 (cit. on pp. 23, 30).

[30] Harald Mehling and Luisa F. Cabeza. *Heat and cold storage with PCM*. Springer Berlin Heidelberg, 2008. ISBN: 978-3-540-68556-2. DOI: 10.1007/978-3-540-68557-9. URL: http://link.springer.com/10.1007/978-3-540-68557-9 (cit. on pp. 25, 26, 28, 61, 64).

[31] Francisco Cabello Núñez. *Thermochemical Energy Storage*. 2020. URL: https://www.restore-dhc.eu/about-restore/thermochemical-energy-storage/# (cit. on p. 26).

[32] Kai Wang, Zhen Qin, Wei Tong, and Chenzhen Ji. «Thermal Energy Storage for Solar Energy Utilization: Fundamentals and Applications». In: ed. by Mansour Al Qubeissi, Ahmad El-kharouf, and Hakan Serhad Soyhan. IntechOpen, 2020. DOI: 10.5772/intechopen.91804. URL: https://doi.org/10.5772/intechopen.91804 (cit. on p. 27).

[33] Ming Liu, N. H. Steven Tay, Stuart Bell, Martin Belusko, Rhys Jacob, Geoffrey Will, Wasim Saman, and Frank Bruno. «Review on concentrating solar power plants and new developments in high temperature thermal energy storage technologies». In: *Renewable and Sustainable Energy Reviews* 53 (Jan. 2016), pp. 1411–1432. ISSN: 1364-0321. DOI: 10.1016/J.RSER.2015.09.026 (cit. on p. 28).

[34] Khaireldin Faraj, Mahmoud Khaled, Jalal Faraj, Farouk Hachem, and Cathy Castelain. «A review on phase change materials for thermal energy storage in buildings: Heating and hybrid applications». In: *Journal of Energy Storage* 33 (Jan. 2021), p. 101913. ISSN: 2352-152X. DOI: 10.1016/J.EST.2020.101913 (cit. on p. 29).

[35] Kamal A R Ismail, Fátima A M Lino, Mohamed Teggar, Müslüm Arıcı, Pedro L O Machado, Thiago A Alves, Ana C O De Paula, and Amani Benhorma. «A Comprehensive Review on Phase Change Materials and Applications in Buildings and Components». In: *ASME Open Journal of Engineering* 1 (Oct. 2022). ISSN: 2770-3495. DOI: 10.1115/1.4055185. URL: https://doi.org/10.1115/1.4055185 (cit. on p. 32).

[36] A. Felix Regin, S. C. Solanki, and J. S. Saini. «Heat transfer characteristics of thermal energy storage system using PCM capsules: A review». In: *Renewable and Sustainable Energy Reviews* 12 (9 Dec. 2008), pp. 2438–2458. ISSN: 1364-0321. DOI: 10.1016/J.RSER.2007.06.009 (cit. on pp. 32, 33).

[37] Pramod B. Salunkhe and Prashant S. Shembekar. «A review on effect of phase change material encapsulation on the thermal performance of a system». In: *Renewable and Sustainable Energy Reviews* 16 (8 Oct. 2012), pp. 5603–5616. ISSN: 1364-0321. DOI: 10.1016/J.RSER.2012.05.037 (cit. on pp. 32–34).

[38] Kang Yanbing, Zhang Yinping, Jiang Yi, and Zhu Yingxin. «A General Model for Analyzing the Thermal Characteristics of a Class of Latent Heat Thermal Energy Storage Systems». In: *Journal of Solar Energy Engineering* 121 (4 Nov. 1999), pp. 185–193. ISSN: 0199-6231. DOI: 10.1115/1.2888165. URL: https://doi.org/10.1115/1.2888165 (cit. on p. 34).

[39] El.Ma. Electronic Machining s.r.l. *Concentratore solare a disco*. 2019. URL: www.elmanet.it (cit. on pp. 37, 38).

[40] C Jiménez et al. «Joining of ceramic matrix composites to high temperature ceramics for thermal protection systems». In: *Journal of the European Ceramic Society* 36 (3 2016), pp. 443–449. ISSN: 0955-2219. DOI: https://doi.org/10.1016/j.jeurceramsoc.2015.09.038. URL: https://www.sciencedirect.com/science/article/pii/S0955221915301576 (cit. on p. 42).

[41] Eugenio Garcia, Andrés Nistal, F Escalera, Amal Khalifa, M Sainz, Maria Osendi, and P Miranzo. «Thermally Sprayed Y2O3-Al2O3-SiO2 Coatings for High-Temperature Protection of SiC Ceramics». In: *Journal of Thermal Spray Technology* 24 (Feb. 2014). DOI: 10.1007/s11666-014-0178-y (cit. on p. 42).

[42] Valentina Casalegno, Luca Ferrari, Maria Jimenez Fuentes, Alessandro De Zanet, Sandro Gianella, Monica Ferraris, and Victor M. Candelario. «High-performance sic–based solar receivers for csp: Component manufacturing and joining». In: 14 (16 Aug. 2021). ISSN: 19961944. DOI: 10.3390/ma14164687 (cit. on p. 42).

[43] Carla Malinverni, Milena Salvo, Maciej Ziętara, Grzegorz Cempura, Adam Kruk, Jonathan Maier, Calvin Prentice, Michael Farnham, and Valentina Casalegno. «A yttrium aluminosilicate glass-ceramic to join SiC/SiC composites». In: *Journal of the European Ceramic Society* (Dec. 2023). ISSN: 09552219. DOI: 10.1016/j.jeurceramsoc.2023.12.095 (cit. on p. 43).

[44] Yahong Zhang and Alexandra Navrotsky. «Thermochemistry of Glasses in the Y2O3-Al2O3-SiO2 System». In: *Journal of the American Ceramic Society* 86 (10 2003), pp. 1727–1732. DOI: https://doi.org/10.1111/j.1151-2916.2003.tb03547.x. URL: https://ceramics.onlinelibrary.wiley.com/doi/abs/10.1111/j.1151-2916.2003.tb03547.x (cit. on p. 43).

[45] Le Wang, Shangwu Fan, Haodong Sun, Biao Ji, Bohan Zheng, Juanli Deng, Litong Zhang, and Laifei Cheng. «Pressure-less joining of SiCf/SiC composites by Y2O3–Al2O3–SiO2 glass: Microstructure and properties». In: *Ceramics International* 46 (17 Dec. 2020), pp. 27046–27056. ISSN: 0272-8842. DOI: 10.1016/J.CERAMINT.2020.07.181 (cit. on p. 43).

[46] COMSOL Multiphysics. *Solar Dish Receiver*. 2021. URL: https://www.comsol.com/model/solar-dish-receiver-19227 (cit. on p. 49).

[47] Christopher Boucher. *How to Model Solar Concentrators with the Ray Optics Module*. 2016. URL: https://www.comsol.it/blogs/how-to-model-solar-concentrators-with-the-ray-optics-module/#ref3 (cit. on p. 50).

[48] Byeongha Moon, Dong-Gwon Jeong, Suyeon Oh, and Jongdae Sohn. «Variation in Solar Limb Darkening Coefficient Estimated from Solar Images Taken by SOHO and SDO». In: *Journal of Astronomy and Space Science* 34 (Mar. 2017), pp. 99–103. DOI: 10.5140/JASS.2017.34.2.99 (cit. on p. 51).

[49] Britannica T. Editors of Encyclopaedia. *limb darkening*. 2018. URL: https://www.britannica.com/science/limb-darkening (cit. on p. 51).

[50] Comsol. *Ray Optics Module User's Guide*. 2018. URL: www.comsol.com/blogs (cit. on p. 51).

[51] Johan Bernander. *Empirical correlations for convective heat transfer coefficients*. URL: https://volupe.se/empirical-correlations-for-convective-heat-transfer-coefficients/ (cit. on p. 56).

[52] *Surface Emissivity Coefficients*. URL: https://www.engineeringtoolbox.com/emissivity-coefficients-d_447.html (cit. on p. 56).

[53] Yong Deng, Jinhong Li, and Hongen Nian. «Expanded Vermiculite: A Promising Natural Encapsulation Material of LiNO 3 , NaNO 3 , and KNO 3 Phase Change Materials for Medium-Temperature Thermal Energy Storage». In: *Advanced Engineering Materials* 20 (Mar. 2018), p. 1800135. DOI: 10.1002/adem.201800135 (cit. on p. 61).

[54] Dominic Groulx and W Ogoh. «Solid-Liquid Phase Change Simulation Applied to a Cylindrical Latent Heat Energy Storage System». In: Mar. 2009 (cit. on p. 61).

[55] *Ciclo Rankine*. URL: https://www.edutecnica.it/macchine/rankine/rankine.htm (cit. on pp. 69, 70).

[56] Siddharth Ramachandran, Naveen Kumar, and Venkata Mallina. «A Comprehensive Perspective of Waste Heat Recovery Potential from Solar Stirling Engines». In: *E3S Web of Conferences* 313 (Mar. 2021), p. 6001. DOI: 10.1051/e3sconf/202131306001 (cit. on p. 70).